ADVANCES IN ATMOSPHERIC SCIENCES, 2026

• Original Paper •

Ocean Heat Content Sets Another Record in 2025※

Yuying PAN[1], Lijing CHENG[*1], John ABRAHAM[2], Kevin E. TRENBERTH[3,4], James REAGAN[5],
Juan DU[6], Zhankun WANG[5], Andrea STORTO[7], Karina VON SCHUCKMANN[8], Yujing ZHU[1],
Michael E. MANN[9], Jiang ZHU[1], Fan WANG[10], Fujiang YU[11], Ricardo LOCARNINI[5], John FASULLO[3],
Boyin HUANG[6], Garrett GRAHAM[12], Xungang YIN[6], Viktor GOURETSKI[1], Fei ZHENG[1], Yuanlong LI[10],
Bin ZHANG[10,13], Liying WAN[11], Xingrong CHEN[11], Dakui WANG[11], Licheng FENG[11], Xiangzhou SONG[14],
Yulong LIU[15], Franco RESEGHETTI[16], Simona SIMONCELLI[16], Gengxin CHEN[17], Rongwang ZHANG[17],
Alexey MISHONOV[5,18], Wangxu WEI[1], Zhetao TAN[19], Guancheng LI[20], Lijuan CAO[21], Lifan CHEN[21],
Huifeng YUAN[22], Kewei LYU[23], Albertus SULAIMAN[24], Michael MAYER[25,26], Huizan WANG[27],
Zhanhong MA[27], Senliang BAO[27], Hengqian YAN[27], Zenghong LIU[28], Chunxue YANG[7],
Xu LIU[11], Zeke HAUSFATHER[29], Flora GUES[30], Xinyi SONG[1],
Miao ZHANG[31,32], and Lin CHEN[31,32]

[1]*State Key Laboratory of Earth System Numerical Modeling and Application*, *Institute of Atmospheric Physics*,
Chinese Academy of Sciences, *Beijing* 100029, *China*
[2]*University of St. Thomas*, *School of Engineering*, *Minnesota* 55105, *USA*
[3]*NSF National Center for Atmospheric Research*, *Boulder*, *Colorado* 80307, *USA*
[4]*University of Auckland*, *Auckland*, *New Zealand*
[5]*National Oceanic and Atmospheric Administration*, *National Centers for Environmental Information*,
Silver Spring, *Maryland* 20910, *USA*
[6]*International Center for Climate and Environment Sciences*, *Institute of Atmospheric Physics*,
Chinese Academy of Sciences, *Beijing* 100029, *China*
[7]*National Research Council (CNR) Institute of Marine Sciences (ISMAR)*, *Rome*, *Italy*
[8]*Mercator Ocean International*, *Toulouse*, *France*
[9]*Department of Earth and Environmental Science*, *University of Pennsylvania*, *Philadelphia*, *Pennsylvania* 19104, *USA*
[10]*Institute of Oceanology*, *Chinese Academy of Sciences*, *Qingdao* 266071, *China*
[11]*National Marine Environmental Forecasting Center*, *Ministry of Natural Resources of China*, *Beijing* 100081, *China*
[12]*North Carolina Institute for Climate Studies (NCICS)*, *North Carolina State University*, *Asheville*, *NC* 28804, *USA*
[13]*Oceanographic Data Center*, *Chinese Academy of Sciences*, *Qingdao* 266071, *China*
[14]*College of Oceanography*, *Hohai University*, *Nanjing* 210098, *China*
[15]*National Marine Data and Information Service*, *Tianjin* 300171, *China*
[16]*Istituto Nazionale di Geofisica e Vulcanologia*, *Sede di Bologna*, *Bologna* 40128, *Italy*
[17]*South China Sea Institute of Oceanology*, *Chinese Academy of Sciences*, *Guangzhou* 510301, *China*
[18]*ESSIC/CISESS-MD*, *University of Maryland*, *College Park*, *MD* 20740, *USA*
[19]*Laboratoire de Météorologie Dynamique*, *Institut Pierre Simon Laplace*, *École Normale Supérieure – Université PSL*,
Paris 75005, *France*
[20]*Eco-Environmental Monitoring and Research Center*, *Pearl River Valley and South China Sea Ecology and Environment Administration*, *Ministry of Ecology and Environment*, *PRC*, *Guangzhou* 510611, *China*
[21]*National Meteorological Information Center*, *China Meteorological Administration*, *Beijing* 100081, *China*
[22]*Computer Network Information Center*, *Chinese Academy of Sciences*, *Beijing* 100083, *China*
[23]*State Key Laboratory of Marine Environmental Science*, *Center for Marine Meteorology and Climate Change*,
College of Ocean and Earth Sciences, *Xiamen University*, *Xiamen* 361005, *China*
[24]*Research Center for Climate and Atmosphere*, *National Research and Innovation Agency* (*BRIN*), *Indonesia*
[25]*Research Department, European Centre for Medium-Range Weather Forecasts*, *Reading RG*2 9*AX*, UK

※ This paper is a contribution to the special topic on Ocean Heat Content Changes.

* Corresponding author: Lijing CHENG
Email: chenglij@mail.iap.ac.cn

[26]*Department of Meteorology and Geophysics*, *University of Vienna*, *Vienna* 1090, *Austria*
[27]*College of Meteorology and Oceanography*, *National University of Defense Technology*, *Changsha*, 410073, *China*
[28]*State Key Laboratory of Satellite Ocean Environment Dynamics*, *Second Institute of Oceanography*,
Ministry of Natural Resources, *Hangzhou* 310012, *China*
[29]*Stripe*, *Inc*., *South San Francisco*, *CA* 94080, *USA*
[30]*CELAD*, *Balma*, *France*
[31]*Key Laboratory of Radiometric Calibration and Validation for Environmental Satellites*, *National Satellite*
Meteorological Center, *China Meteorological Administration*, *Beijing* 100081, *China*
[32]*Innovation Center for FengYun Meteorological Satellite (FYSIC)*, *Beijing* 100081, *China*

(Received 16 December 2025; revised 7 January 2026; accepted 8 January 2026)

ABSTRACT

Global ocean warming continued unabated in 2025 in response to increased greenhouse gas concentrations and recent reductions in sulfate aerosols, reflecting the long-term accumulation of heat within the climate system, with conditions evolving toward La Niña during the year. In 2025, global upper 2000 m ocean heat content (OHC) increased by ~23 ± 8 ZJ relative to 2024 according to IAP/CAS estimates. CIGAR-RT, and Copernicus Marine data confirm the continued ocean heat gain. Regionally, about 33% of the global ocean area ranked among its historical (1958-2025) top three warmest conditions, while about 57% fell within the top five, including the tropical and South Atlantic Ocean, Mediterranean Sea, North Indian Ocean, and Southern Oceans, underscoring the broad ocean warming across basins. Multiple datasets consistently indicate ocean warming, as measured by 0–2000 m OHC, increased from 0.14 ± 0.03 W m^{-2} (10 yr)$^{-1}$ during 1960–2025 to 0.32 ± 0.14 W m^{-2} (10 yr)$^{-1}$ during 2005–2025 (IAP/CAS), the latter being consistent with EEI (Earth's Energy Imbalance) estimates within uncertainties. In contrast, the global annual mean sea surface temperature (SST) in 2025 was 0.49°C above the 1981–2010 baseline and 0.12 ± 0.03°C lower than in 2024 (IAP/CAS; similar in CMA-SST, FY3 MWRI SST, ERSSTv5 and Copernicus Marine data), consistent with the development of La Niña conditions, but still ranking as the third-warmest year on record.

Key words: ocean heat content, sea surface temperature, ocean temperature, global warming, climate change

Citation: Pan, Y. Y., and Coauthors, 2026: Ocean heat content sets another record in 2025. *Adv. Atmos. Sci.*, https://doi.org/10.1007/s00376-026-5876-0.

Article Highlights:

- In 2025, the global upper 2000 m OHC was the highest recorded by modern instruments, ~23 ZJ higher than the 2024 value.
- The 2025 annual mean global SST was 0.12°C lower than in 2024, but ranked as third warmest in the instrumental record.
- Record-high OHC in 2025 arose in the tropical and South Atlantic, Mediterranean Sea, North Indian, and Southern Oceans.

1. Introduction

The year 2025 represents another step in an ongoing sequence of remarkable changes observed in Earth's climate system. In this paper we focus on the 2025 ocean temperatures, especially the ocean heat content (OHC), which has repeatedly reached record-high levels in recent years.

Although global mean surface temperature (GMST) in 2025 was slightly lower than in 2024 and, for several months, also lower than during the strong El Niño–driven warmth of late 2023, it nevertheless remained exceptionally high by historical standards. Based on an assessment of January–November data from Berkeley Earth (Rohde and Hausfather, 2020), NASA GISTEMP (Lenssen et al., 2019), NOAA-GlobalTemp v6 (Yin et al., 2024), HadCRUT5 (Morice et al., 2021), and ERA5 (Hersbach et al., 2023), GMST in 2025 is expected to approximately tie with 2023 as the second-warmest year since records began in 1850, continuing the extraordinary string of record-warm years that has characterized the past decade. With 2025 extending the warmest 11-year period on record (2015–2025), this marks an unparalleled sequence of record and near-record global surface temperatures in the observational era.

This persistent, though slightly moderated, warmth in GMST occurred alongside continued changes across other components of the climate system (Hansen et al., 2011; IPCC, 2021). Greenhouse gas concentrations reached record levels in 2025 (Judd et al., 2024; Blunden et al., 2025), and real-time observations indicate that this upward trend continued through 2025, reinforcing the long-term warming trajectory. Large-scale climate drivers also evolved: the strong El

Niño of late 2023 fully dissipated by early 2025, giving way to weak La Niña conditions, yet many regions still experienced elevated temperatures relative to the pre-2023 climate due to the accumulated energy in the Earth system. Cryospheric indicators reflected this sustained warming as well, with Arctic and Antarctic sea-ice extents in 2025 remaining well below the 1981–2010 climatology; the Arctic reached the lowest annual maximum extent and Antarctica recorded the third-lowest annual minimum and maximum extents in the satellite era. Year-to-date observations also show that both the Greenland and Antarctic ice sheets reached record-low mass levels, and new studies suggest that portions of these ice sheets may already have crossed critical climate tipping points (Stokes et al., 2025). These record-low mass levels imply continued long-term contributions to global sea-level rise, although La Niña-related increases in land water storage temporarily moderate the rate of sea-level rise. Together, these factors helped shape the patterns of regional climate anomalies and contributed to the occurrence and severity of extreme events across the globe during the year.

During 2025 extreme climate-related events caused widespread societal and ecological impacts across the globe (Brett et al., 2025; Cologna et al., 2025). In South and Southeast Asia, exceptionally intense monsoon rains triggered catastrophic flooding, with some regions receiving up to 800 mm of rainfall over a five-day period in July. Floods killed more than 1350 people in Indonesia, Sri Lanka, Thailand and Vietnam in November. Hundreds more were missing and millions have been displaced. Central China also experienced severe mountain floods and landslides in July, forcing large-scale evacuations and causing substantial infrastructure damage. In the United States, a catastrophic flash flood in Central Texas over the 4 July weekend, triggered by record-breaking rainfall, resulted in at least 138 fatalities, highlighting the escalating risks associated with rapidly intensifying storm systems in a warming climate. Elsewhere, Nigeria and neighboring West African regions suffered damaging flash floods that displaced thousands of people. In western and southern Europe, a persistent summer heat dome drove surface air temperatures over land above 48°C and fueled extensive wildfires. In North America, a series of powerful convective storms produced more than 150 tornadoes, while prolonged drought and early-season heat contributed to over 1200 wildfires that burned more than five million hectares in Canada (Copernicus Climate Change Service, 2025; Ripple et al., 2025).

The widespread extreme events of 2025 arose within a climate system increasingly shaped by long-term heat accumulation, with natural variability amplified by a much warmer atmosphere holding more water vapor (Trenberth et al., 2003, 2011). Central to this long-term warming is the persistent Earth's Energy Imbalance (EEI), which reflects the net surplus of incoming over outgoing energy at the top of the atmosphere and has remained strongly positive in recent decades (Loeb et al., 2021, 2022; Hakuba et al., 2024).

With atmospheric greenhouse gases at record levels and the oceans absorbing more than 90% of the excess heat trapped by these gases (Trenberth et al., 2014; von Schuckmann et al., 2020, 2023; Cheng et al., 2022a), the thermal state of the ocean plays an important role in modulating global and regional climate impacts, primarily through increased atmospheric moisture and enhanced energy availability (Trenberth et al., 2025). Changes in OHC reflect the integrated storage of this excess energy and are governed by the energy exchange across the air–sea interface (Yu and Weller, 2007). Although direct surface flux estimates are subject to considerable uncertainties (Zhang et al., 2018, 2023), recent energy-budget-based approaches that combine top-of-atmosphere (TOA) radiation observations with atmospheric energy divergence provide more robust constraints on the net surface heat flux and its role in OHC variability and long-term warming (Mayer et al. 2022, 2024; Trenberth et al., 2025).

Because OHC changes are far less sensitive to short-term atmospheric variability and ENSO-related fluctuations than GMST, they provide one of the most robust indicators of long-term climate change (Li et al., 2006; Cheng et al., 2017b, 2025; Hakuba et al., 2024). Observational records further show that OHC has increased robustly over the full observational period (Cheng et al., 2017a, 2019; Li et al., 2023; Minière et al., 2023), underscoring the persistent buildup of excess heat within the Earth system. The elevated OHC influences the frequency and intensity of marine heatwaves (Capotondi et al., 2024; Dong et al., 2025; Marcos et al., 2025), alters atmospheric circulation (Li et al., 2012; Thomas and Liu, 2025), increases evaporation and moisture availability (Ma et al., 2020; Allan, 2023), and contributes to both stronger precipitation extremes and more favorable conditions for rapid tropical cyclone intensification (Trenberth et al., 2018; Li et al., 2020). The persistence of anomalously warm subsurface and basin-wide ocean conditions in 2025 has also played a critical role in shaping hydrological and thermodynamic extremes across the globe.

To deliver an up-to-date assessment of ocean warming and inform climate-related applications, this study synthesizes multiple datasets from leading international data centers to examine global and regional variations in OHC and SST through 2025. The datasets and methods are described in detail in section 2. Section 3 provides an analysis of the changes and increasing rates of global OHC and SST. Sections 4 and 5 examine the spatial patterns of OHC and SST anomalies, respectively. Regional OHC anomalies and associated hotspot regions are discussed in section 6, and section 7 summarizes the main findings and broader implications of the observed changes in 2025.

2. Advances in data and processing

2.1. *OHC data*

The global OHC estimates used in this study are based on three gridded observational products and an ocean reanalysis product. The observational products are: (1) the Institute of Atmospheric Physics (IAP) at the Chinese Academy of Sciences (CAS) (Cheng et al., 2017a, 2024a; Zhang et al., 2024a; Tan et al., 2025a); (2) Copernicus Marine (von Schuckmann and Le Traon, 2011); and (3) National Centers for Environmental Information (NCEI) at the National Oceanic and Atmospheric Administration (NOAA) (Levitus et al., 2012). The ocean reanalysis product is CIGAR [CNR ISMAR Global historical Reanalysis (Storto and Yang, 2024)].

The IAP/CAS OHC analysis is mainly based on in situ subsurface temperature profiles from the World Ocean Database (WOD; Boyer et al., 2018; Mishonov et al., 2024) and from post-quality-controlled Argo measurements distributed through China Argo Real-time Data Center (Liu et al., 2021). In addition, the IAP/CAS analysis incorporates 107 623 non-WOD profiles. These additional observations are mainly distributed in the Northwest Pacific, the Indonesian Throughflow (ITF) region, the marginal seas around China, and parts of the Arctic during 1980–2020, providing enhanced coverage in historically under-sampled regions. The product provides monthly 1° × 1° gridded fields for the global ocean from the surface to 6000 m deep.

For this year's release, the IAP/CAS product retains the same core data sources, mapping scheme, and processing framework as previous versions (Cheng et al., 2025), with only small refinements to the quality-control (QC) system (Tan et al., 2023). These refinements include a modest improvement to the instrument maximum depth check and an additional, more precise iterative gradient–spike check until no further threshold-exceeding vertical gradients or spikes are detected in the QC'd profile (see details in Tan et al., 2025a). Because these updates target only specific QC modules, the resulting changes to global OHC and SST values relative to the 2024 release are very small, and the two versions show a high degree of continuity (Cheng et al., 2025).

The Copernicus Marine OHC product for 2005–2025 is derived using the same methodology and data sources as last year's release (Cheng et al., 2025), relying exclusively on Argo temperature profiles from the CORA in situ dataset (Szekely et al., 2024) and a weighted box-averaging approach (von Schuckmann and Le Traon, 2011; EU Copernicus Marine Service Product, 2023a).

The CIGAR OHC reanalysis product used this year follows the ensemble framework described by Storto and Yang (2024), with several upgrades relative to last year's release (Cheng et al., 2025). Specifically, the real-time extension (CIGAR–RT) has been expanded from four to eight ensemble members updated in real time, out of the total of 42 ensemble members of CIGAR. For the final month of 2025, Argo observations are ingested directly from the Coriolis/Ifremer Global Data Assembly Centers (GDAC) and replace the EN4 dataset. Additionally, the ensemble design incorporates alternative SST products for surface relaxation, with individual ensemble members using either COBEv2 SST (Ishii et al., 2005) or UKMO HadISST (Rayner et al., 2003) statistically interpolated SST fields, together with a deep-ocean, large-scale model bias correction scheme (Storto et al., 2016). The ensemble spread thus explicitly accounts for differences in the ingested SST dataset, further to the stochastic modulation of model parameters and observations.

The NOAA/NCEI global OHC product is based on the WOD, which integrates a wide range of in situ temperature profile observations, including ship-based measurements, XBTs (expendable bathythermographs), MBTs (mechanical bathythermographs), and Argo floats. Standard QC procedures and established bias-correction schemes are applied to address instrument-related systematic errors, particularly those associated with XBT and MBT measurements (Levitus et al., 2012; Boyer et al., 2018). Methodological differences between the NOAA/NCEI and IAP/CAS OHC products have been documented and compared in Cheng et al. (2024b).

To evaluate Mediterranean OHC changes, we also employ the regional reanalysis dataset CMS-MEDREA (Escudier et al., 2021; Nigam et al., 2021). The CMS-MEDREA regional reanalysis integrates a range of in situ temperature profile observations, including XBT, CTD (conductivity, temperature, and depth), and Argo measurements, complemented by satellite along-track sea-level anomaly information. These observational datasets are drawn from CMS (Copernicus Marine Service) and the SeaDataNet archive (https://www.seadatanet.org/) and are assimilated within a numerical ocean modeling system based on NEMO coupled with a variational data assimilation framework (Escudier et al., 2020, 2021). The resulting product is provided on a high-resolution grid with a horizontal spacing of 1/24° (approximately 4–5 km) and 141 unevenly distributed vertical levels.

2.2. *SST data*

SST estimates in this analysis are obtained from five products: (1) the first layer (1 m) of the IAP/CAS ocean temperature gridded product; (2) the China's FengYun-3 Microwave Radiation Imager Sea Surface Temperature (FY3 MWRI SST) product from 2011 to the present; (3) the China Meteorological Administration Sea Surface Temperature (CMA-SST) dataset, which is global monthly SST dataset on a 2° × 2° grid from January 1850 to the present (Chen et al., 2021, 2025a); (4) the Extended Reconstructed Sea Surface Temperature (ERSST) dataset, which is a global monthly SST dataset on a 2° × 2° grid from January 1854 to the present (Huang et al., 2017, 2020); and (5) the Copernicus Marine (OSTIA, Good et al., 2020; EU Copernicus Marine Service Product, 2023b, 2023c) global SST reprocessed product from 1982 to present.

The Microwave Radiation Imager (MWRI) is the first-generation microwave imager onboard China's FengYun-3 (FY-3) meteorological satellites (Chen et al., 2025b). FY3 MWRI SST products are derived from an empirical algorithm, where brightness temperature (BT) products and in situ SST data are used to train the retrieval model. Based on reprocessed BT products and an improved retrieval algorithm, the FY3 MWRI SST data from the FY-3B, FY-3C, and FY-3D satellites have been generated with quality flags (Zhang et al., 2024b). Over ice-covered regions, a freezing point–based proxy algorithm is employed for ice-SST retrieval (Huang et al., 2021). To avoid the impact of diurnal variations, the reprocessed nighttime monthly SST products with a spatial resolution of 25 km are utilized in this study.

The CMA-SST dataset provides a global monthly SST dataset on a 2° × 2° grid from January 1850 to the present. It is compiled from ship and buoy SST observations of a newly developed integrated dataset, with denser in situ observations than ICOADS3.0. For ship SST records before 2010, a large-scale statistical technique is performed via comparison with the nighttime marine air temperature (NMAT) dataset, followed by readjustment using the 1990–2010 global mean offset between NMAT- and buoy-derived bias estimates. For ship SST data from 2010 onward, adjustment is conducted against the global mean of ship-buoy SST discrepancies. Thereafter, CMA-SST is generated by separate reconstruction and combination of the SST field's low- and high-frequency components: the low-frequency component is obtained via spatiotemporal running averaging to capture large-scale SST characteristics; the high-frequency component is calculated as the residual of original observations minus the low-frequency component, then fitted using EOT (empirical orthogonal teleconnection) modes to obtain a full-coverage reconstruction (Chen et al., 2021, 2025a).

ERSST.v5 (version 5 of ERSST) and OSTIA (Copernicus Marine OSTIA) SST products (EU Copernicus Marine Service Product, 2023b, 2023c) used in this study follow the same data sources and methodological frameworks as in last year's assessment (Cheng et al., 2025), with their temporal coverage extended to the present.

2.3. *EEI data*

The EEI data used in this study are from the Clouds and the Earth's Radiant Energy System (CERES) Energy Balanced and Filled (EBAF) Ed4.2 product (Loeb et al., 2018), which provides globally consistent TOA radiative fluxes. CERES instruments have provided continuous broadband radiation measurements since March 2000. The CERES EBAF Ed4.2 record delivers consistent monthly mean shortwave, longwave, and net radiative fluxes at the TOA, and is widely used as a reference dataset for studies of Earth's radiation budget. In this study, owing to the data availability, we use the period from March 2000 to September 2025.

2.4. *Trend and uncertainty calculation*

Trends in OHC are estimated using the locally weighted scatterplot smoothing (LOWESS) approach following Cheng et al. (2022b), which reduces the effects of high-frequency climate variability such as ENSO. First, each annual OHC time series is smoothed using a 25-year LOWESS filter, corresponding to an effective smoothing scale of approximately 15 years. The long-term trend is then quantified as the difference between the smoothed values at the start and end years, divided by the length of the period:

$$\text{OHC Trend} = \frac{\widetilde{\text{OHC}}(t_2) - \widetilde{\text{OHC}}(t_1)}{t_2 - t_1}\,, \qquad (1)$$

where $\widetilde{\text{OHC}}$ is the LOWESS-smoothed annual OHC, t_1 and t_2 are the beginning and end of the analysis period. This method is much more robust and reproducible than fitting linear or quadratic trends.

Uncertainty in the trend estimates reflects multiple factors, including mapping methods and data sampling, instrumental errors and bias corrections, climatological choices, QC procedures, and the trend-calculation method itself. Because these processing elements differ across datasets and time periods, the internal uncertainty is assessed separately using the Monte Carlo surrogate approach following Cheng et al. (2022b). For each time series, 1000 surrogate realizations are generated by perturbing annual values with Gaussian noise derived from the observational error estimates. LOWESS smoothing is then applied to each surrogate, and a corresponding trend estimate, OHC Trend, is calculated. The internal uncertainty is taken as the 95% confidence interval, computed as ± 2 times the standard deviation of these 1000 trend estimates, and represents the uncertainty of each individual dataset.

2.5. *Fifteen-year ocean warming rate and uncertainty calculation*

The 15-year heating rates are calculated with a linear least-squares regression over a moving 15-year window following Cheng et al. (2024c). The associated uncertainties are derived from the spread of 15-year heating rates across ensembles for each product. For IAP/CAS, we use a 918-member large ensemble, constructed from eight groups of error sources, including alternative QC procedures, XBT bias-correction schemes, bottle bias corrections, APB (Autonomous Pinniped Bathythermograph) bias corrections, MBT bias corrections, choices of climatology, vertical interpolation methods, and mapping plus instrumental errors. For CIGAR-RT and Copernicus Marine, we generate 1000-member synthetic ensembles using Monte Carlo perturbations based on their annual OHC uncertainties, thereby sampling the plausible realizations of each product consistent with its error estimates. For IAP/CAS, CIGAR-RT and Copernicus Marine, the uncertainty in each 15-year window is quantified as ± 2 standard deviations of the ensemble-derived heating rates, as described above.

2.6. *Change in rate and uncertainty calculation*

The change in OHC rate is calculated via a quadratic regression on OHC annual time series by taking twice the quadratic term. Specifically, for each product and period of interest, we model the annual OHC anomalies as

$$y_i = \beta_0 + \beta_1 \widetilde{t_i} + \beta_2 \widetilde{t_i}^2\,, \qquad (2)$$

where y_i denotes the annual mean OHC anomaly at time t_i, β_0 is the intercept, $\beta_1$is the coefficient of the linear term, and β_2 is the quadratic coefficient. The time variable $\widetilde{t_i} = t_i - \bar{t}$ is time measured relative to the midpoint $\bar{t}$ of the fitting interval. The change in OHC rate a is then defined as

$$a = 2\beta_2 \,. \tag{3}$$

The uncertainty of the change in OHC rate is following the error–covariance propagation approach consistent with Ablain et al. (2019) and Minière et al. (2023). Let $\boldsymbol{X}$ denote the $N \times 3$ design matrix with columns $\left[1, \widetilde{t_i}, \widetilde{t_i^2}\right]$, in which N is the length of the annual OHC time series used in the regression. The central estimate of the regression coefficients is obtained from the ordinary least-squares (OLS) solution:

$$\widehat{\boldsymbol{\beta}} = (\mathbf{X}^{\mathrm{T}}\mathbf{X})^{-1}\mathbf{X}^{\mathrm{T}}y \,. \tag{4}$$

The regression coefficients are estimated using OLS, while the effect of temporally correlated errors is accounted for through the error–covariance propagation. Because the OHC ensemble for each product is available in section 2.5, we first estimate the $N \times N$ error variance–covariance matrix $\boldsymbol{\Sigma}$ of annual OHC anomalies from the corresponding ensemble. $\boldsymbol{\Sigma}$ captures both the error variance of individual years and the temporal correlation of the errors. The covariance matrix of the regression coefficients is then given by

$$\mathrm{Cov}\left(\widehat{\boldsymbol{\beta}}\right) = \left(\mathbf{X}^{\mathrm{T}}\mathbf{X}\right)^{-1}\left(\mathbf{X}^{\mathrm{T}}\boldsymbol{\Sigma}\mathbf{X}\right)\left(\mathbf{X}^{\mathrm{T}}\mathbf{X}\right)^{-1} , \tag{5}$$

and the variance of the change in OHC rate, σ^2, can be calculated as

$$\sigma^2 = 4 \times \left[\mathrm{Cov}\left(\widehat{\boldsymbol{\beta}}\right)\right]_{33} , \tag{6}$$

where $\left[\mathrm{Cov}\left(\widehat{\boldsymbol{\beta}}\right)\right]_{33}$ denotes the (3,3) element of the covariance matrix of the regression coefficients, corresponding to the variance of the quadratic regression coefficient $\boldsymbol{\beta}_2$. Finally, the uncertainty of the change in OHC rate can be obtained as 2σ.

3. The global ocean state in 2025

3.1. *OHC*

Long-term observational records reveal a clear and sustained increase in global upper OHC since the late 1950s (Fig. 1). Despite differences in input data and processing approaches, all three datasets consistently show marked ocean warming throughout the upper 2000 m. According to the IAP/CAS analysis, the global ocean has gained heat at an average rate of 6.6 ± 0.3 ZJ yr^{-1} (1 ZJ $\mathrm{yr}^{-1} \approx 0.06$ W m^{-2}) over the full period 1958–2025. The pace of warming has strengthened substantially over time. During 1958–1985, the IAP record indicates a trend of 2.9 ± 0.5 ZJ yr^{-1}, whereas after 1986 the rate increases to roughly 9.2 ± 0.4 ZJ yr^{-1}, representing over a threefold increase. The most recent period shows even faster warming. Since 2007, the improved global coverage of subsurface ocean observations allowed more accurate estimates of OHC changes. During the period 2007–2025, upper 2000 m OHC has increased by11.4 ± 1.0 ZJ yr^{-1} in the IAP/CAS dataset, 11.3 ± 1.3 ZJ yr^{-1}in Copernicus Marine, 12.9 ± 0.8 ZJ yr^{-1} in NCEI/NOAA (updated to June 2025), and 12.2 ± 1.8 ZJ yr^{-1} in CIGAR-RT, highlighting a pronounced multi-decadal acceleration of ocean warming (Cheng et al., 2019, 2024c; Loeb et al., 2022; Minière et al., 2023; Storto and Yang, 2024). The strong agreement among datasets over the past two decades reflects improvements inobserving system coverage and quality (green bars in Fig. 1),largely driven by the deployment of the Argo program, and thereby results in enhanced confidence in recent OHC trends.

The 2025 upper 2000 m OHC exceeds the 2024 value by 23 ± 8 ZJ (IAP/CAS), 20 ± 3 ZJ (CIGAR-RT), 13 ± 5 ZJ (NCEI/NOAA, updated to June 2025) and 70 ± 39 ZJ (Copernicus Marine, which indicates a larger increase but with substantial uncertainty due to the use of near-real time data), making 2025 the hottest year on record for OHC (Figs. 1, 2, Table 1). OHC increased sharply from late 2024 (around October) through September 2025, and notable differences among products indicate differences in the data processing procedure. We suggest a careful investigation into ocean data processing techniques (e.g., QC, bias correction, mapping) to identify best practices and reconcile these estimates. Besides anthropogenic drivers of ocean heat accumulation, the development of La Niña also partly contributes to this heat accumulation from 2024 to 2025, because the anomalous cold near-surface condition in the tropical eastern Pacific leads to more heat input into the ocean compared with normal conditions (Cheng et al., 2022c). Furthermore, according to both the IAP/CAS and CIGAR-RT datasets, OHC has reached a new record for nine consecutive years (2017–25), representing the longest sequence of consecutive annual OHC records in the observational era.

The record-high OHC in 2025 signals robust climate warming. Different data products provide evidence for a long-term increase in ocean heat uptake, with the ocean warming rate rising over time (Fig. 3). Over 1960–2025, the IAP/CAS dataset shows a global value of 0.14 ± 0.03 W m^{-2} (10 yr)$^{-1}$ (averaged over the global surface area), while the CIGAR-RT yields a comparable estimate of 0.16 ± 0.02 W m^{-2} (10 yr)$^{-1}$. The estimates in the recent observing era (~2005) are considered more reliable, owing to the widespread availability of Argo observations. During 2005–2025, IAP/CAS indicates a value of 0.32 ± 0.14 W m^{-2} (10 yr)$^{-1}$, broadly consistent with the rate of 0.32 ± 0.10 W m^{-2} (10 yr)$^{-1}$ in CIGAR-RT, and 0.46 ± 0.26 W m^{-2} (10 yr)$^{-1}$ in Copernicus Marine, with agreement among the datasets within their respective uncertainty ranges (Fig. 3, Table 2).

As ocean warming provides direct evidence that the climate system is out of thermal equilibrium and accumulating heat, the EEI offers an additional supporting indicator. Based on CERES observations and assuming that more than 90% of the excess energy is absorbed by the ocean, the EEI-implied ocean heat uptake exhibits an increase of 0.37 ± 0.20 W m^{-2} (10 yr)$^{-1}$ over the period 2005 through September

(a) Global ocean heat content in the upper 2000 m (IAP/CAS)

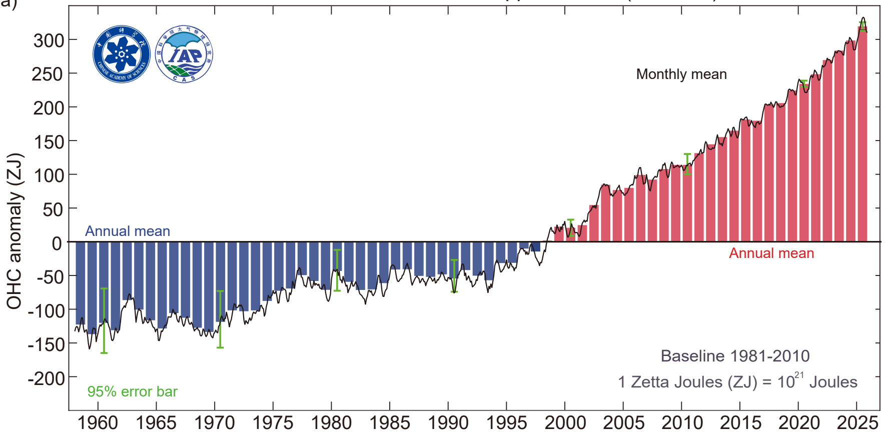

(b) Global ocean heat content in the upper 2000 m (CIGAR-RT reanalysis)

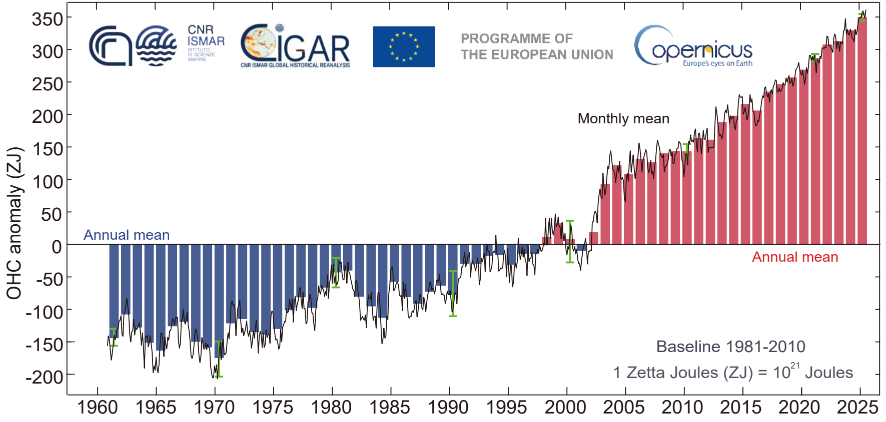

(c) Global ocean heat content in the upper 2000 m (Copernicus Marine)

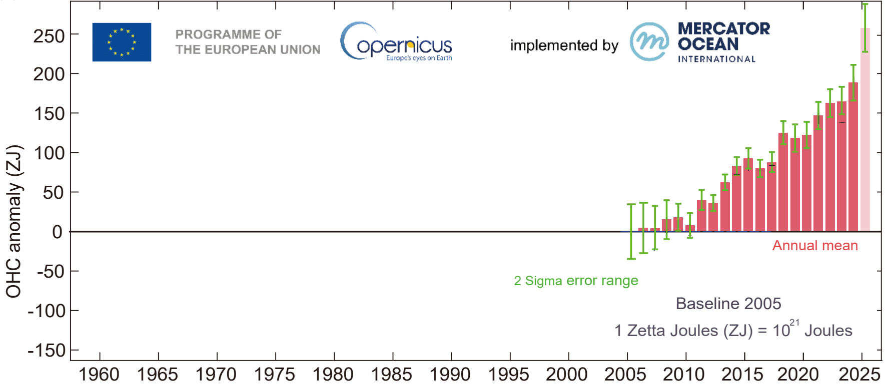

Fig. 1. Global upper 2000 m OHC from 1958 through 2025 according to (a) IAP/CAS, (b) CIGAR-RT (from 1961 through 2025), and (c) Copernicus Marine (from 2005 through 2025) (1 ZJ = 10^{21} J). In panels (a) and (b), the black curves represent monthly time series, while the histograms show annual anomalies. In panel (c), 2025 data are preliminary (near real-time), plotted separately (light pink), and might be not fully representative. All time series are referenced to the 1981–2010 climatology for the IAP/CAS and CIGAR-RT products, and to a 2005 reference level for the Copernicus Marine product. For reference, the 2005 OHC values relative to the 1981–2010 baseline are 78 ZJ for IAP/CAS and 104 ZJ for CIGAR-RT. Uncertainty estimates from the different datasets are illustrated by the green bars. Note that the *y*-axis scales differ among panels.

2025 (Fig. 3, Table 2). Collectively, these results demonstrate a coherent picture of an intensifying ocean warming, consistent with previous assessments (Cheng et al., 2019, 2024a, 2024c; Loeb et al., 2021).

Table 1. Ranked order of the five hottest years of the world's oceans since 1955. The OHC values are for the upper 2000 m in units of ZJ, relative to the 1981–2010 average. ΔOHC denotes the year-to-year change in OHC relative to the previous year in units of ZJ. Note that the IAP/CAS values from 2021–2024 differ from the previous release by 1–2 ZJ [Table 1 in Cheng et al. (2025)]. The incorporation of newly available WOD temperature profiles from September 2024 through July 2025 increases the difference between the 2024 and 2023 OHC estimates, while the modest updates to the QC procedures introduce minor adjustments to the IAP/CAS 1981–2010 baseline. CIGAR data slightly differ from previous release estimates as well [Table 1 in Cheng et al. (2025)], owing to an ensemble extension of the real-time reanalysis system. For NCEI/NOAA, the current data extend through June 2025.

		IAP/CAS		CIGAR-RT		NCEI/NOAA	
Rank	Year	OHC (units: ZJ)	ΔOHC (units: ZJ)	OHC (units: ZJ)	ΔOHC (units: ZJ)	OHC (units: ZJ)	ΔOHC (units: ZJ)
1	2025	317	23	346	20	306	13
2	2024	294	13	326	17	293	11
3	2023	281	15	309	5	282	19
4	2022	266	19	304	21	263	14
5	2021	247	15	283	18	249	18

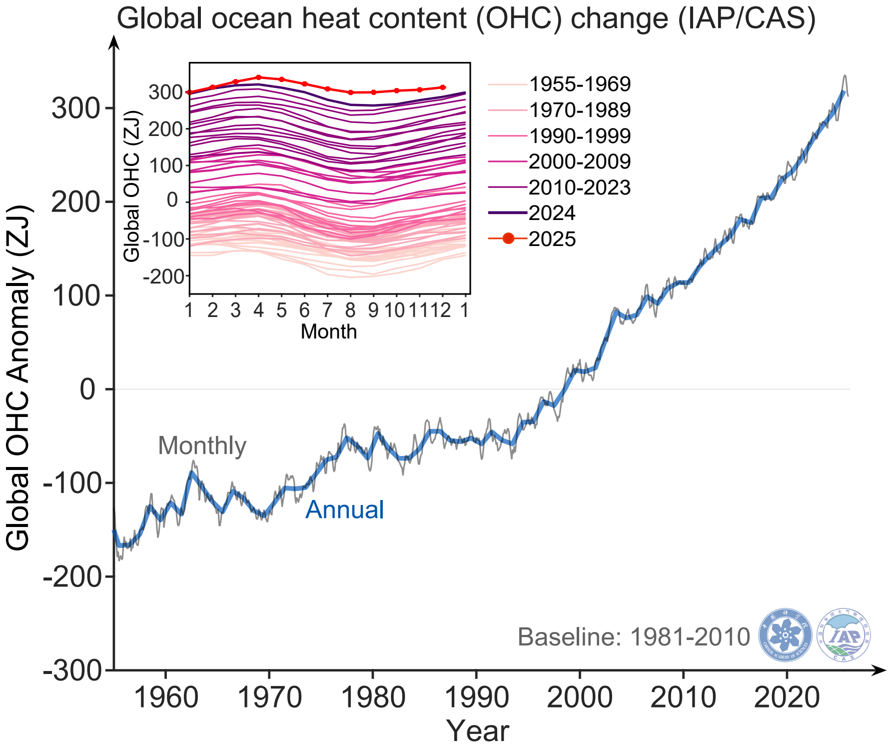

Fig. 2. Global upper 2000 m OHC changes from 1955 through 2025 (units: ZJ). The thick lines denote the annual values, while the thin lines represent the monthly values. The OHC anomalies are relative to the 1981–2010 baseline. The inner box shows the intra-annual variation of OHC, with 2025 values highlighted in red.

3.2. *SST*

Global mean SST has risen markedly since at least the mid-20th century (Fig. 4). Over the period 1958–2025, the mean SST trend is 0.12 ± 0.01°C (10 yr)$^{-1}$ for IAP/CAS, 0.13 ± 0.01°C (10 yr)$^{-1}$ for CMA-SST, and 0.12 ± 0.02°C (10 yr)$^{-1}$ for ERSST data. Satellite-based estimates from the Copernicus Marine OSTIA product also indicate a warming rate of 0.15 ± 0.02°C (10 yr)$^{-1}$ since 1982, in close agreement with IAP/CAS, CMA-SST and ERSST results over the same period. Compared with OHC changes, SST variations exhibit substantially larger interannual variability, reflecting the strong influence of atmospheric forcing and internal climate variability (Fig. 4 versus Figs. 1, 2).

Global mean SST declined through the second half of 2024, and 2025 maintained this relatively low state rather than returning to the exceptional warmth of 2023–24 (Fig. 4, IAP/CAS). The continued cooling toward the end of 2025 partly reflects the development of La Niña conditions, which favor enhanced equatorial upwelling and reduced surface temperatures across the tropical Pacific. In line with these changes, the global annual mean SST in 2025 was 0.12°C ± 0.03°C lower than in 2024 based on IAP/CAS esti-

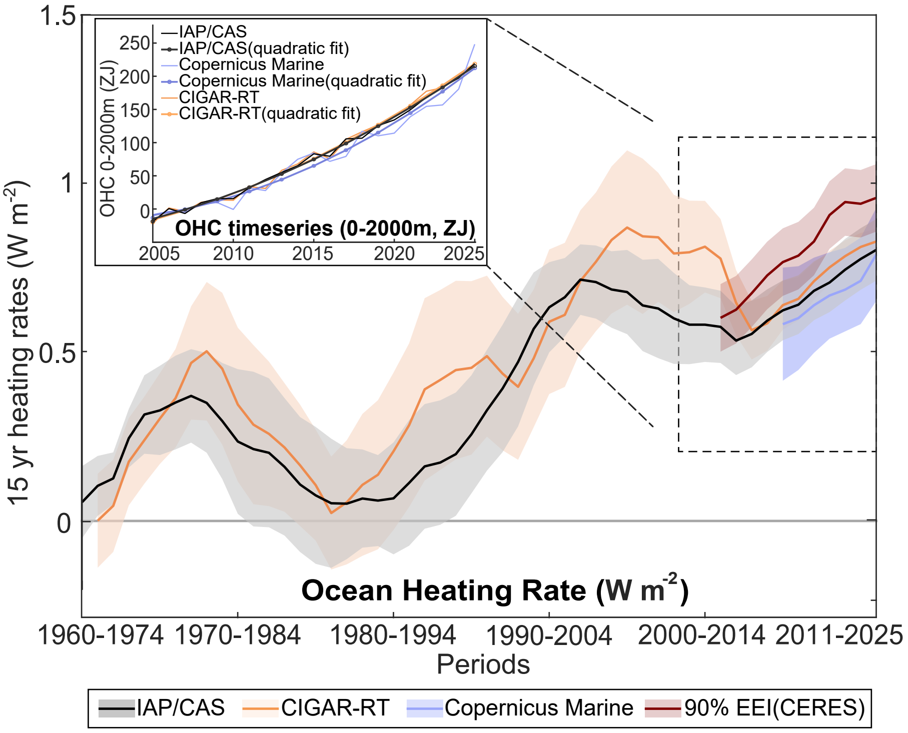

Fig. 3. Running 15-year ocean heating rates and uncertainties for the IAP/CAS, CIGAR-RT, Copernicus Marine, and CERES satellite observations of the net TOA radiation (units: W m^{-2}). For the observational datasets and reanalysis data, uncertainties are represented by twice the standard deviation of ensemble warming rates for each product. All heating rates are expressed per unit area of Earth's surface (5.1 × 10^{14} m^2). The inset displays the annual OHC time series (colored solid lines) and the quadratic fits to the OHC (colored solid lines with circle markers) over 2005–2025, relative to the 2005–2009 baseline (units: ZJ).

Table 2. The change of upper 2000 m OHC rate [quadratic fit; units: W m^{-2} (10 yr)$^{-1}$] from 1960 to 2025 and from 2005 to 2025.

Dataset	Period 1960–2025 [units: W m^{-2} (10 yr)$^{-1}$]	Period 2005–2025 [units: W m^{-2} (10 yr)$^{-1}$]
IAP/CAS	0.14 ± 0.03	0.32 ± 0.14
CIGAR-RT	0.16 ± 0.02	0.32 ± 0.10
Copernicus Marine	\	0.46 ± 0.26
CERES	\	0.37 ± 0.20 (up to September 2025)

mates, to be compared with decreases of 0.08°C (ERSST), 0.09°C (Copernicus Marine), 0.08°C (FY3 MWRI SST) and 0.08°C (CMA-SST) (Fig. 4). Despite this decline, the 2025 global annual mean SST remained 0.49°C ± 0.02°C (IAP/CAS) above the 1981–2010 climatological baseline (0.50°C for ERSST, 0.49°C for Copernicus Marine, 0.50°C for CMA-SST), ranking as the third highest on record across all four datasets, and remained far above the pre-industrial baseline (Table 3). Low SST can also contribute to ocean heat uptake as it lowers tropospheric temperatures and thus outgoing longwave radiation.

4. Spatial patterns of OHC changes in 2025

The 2025 upper 2000 m OHC anomaly pattern relative to the 1981–2010 climatology (Fig. 5a) reflects the well-established structure of long-term ocean warming driven by anthropogenic forcing and large-scale circulation (Cheng et al., 2022a; Latif et al., 2023; Trenberth et al., 2025). Strong positive anomalies persist in the Atlantic, North Pacific, the Indo-Pacific warm pool, and along the northern flank of the Antarctic Circumpolar Current (ACC), consistent with previously documented regions of enhanced heat uptake and redistribution (Cheng et al., 2024b, 2025; Trenberth et al., 2025). A detailed synthesis of the mechanisms governing these long-term OHC warming structures is provided in Cheng et al. (2022a).

Superimposed on this long-term pattern, a weak cooling signal of up to −1 GJ m^{-2} (1 GJ = 10^9 J) emerges in the central equatorial Pacific, consistent with thermocline shoaling and cold subsurface water upwelling under the developing La Niña conditions in 2025 (Figs. 5a, b). This cooling reflects the basin-scale adjustment of the tropical Pacific following

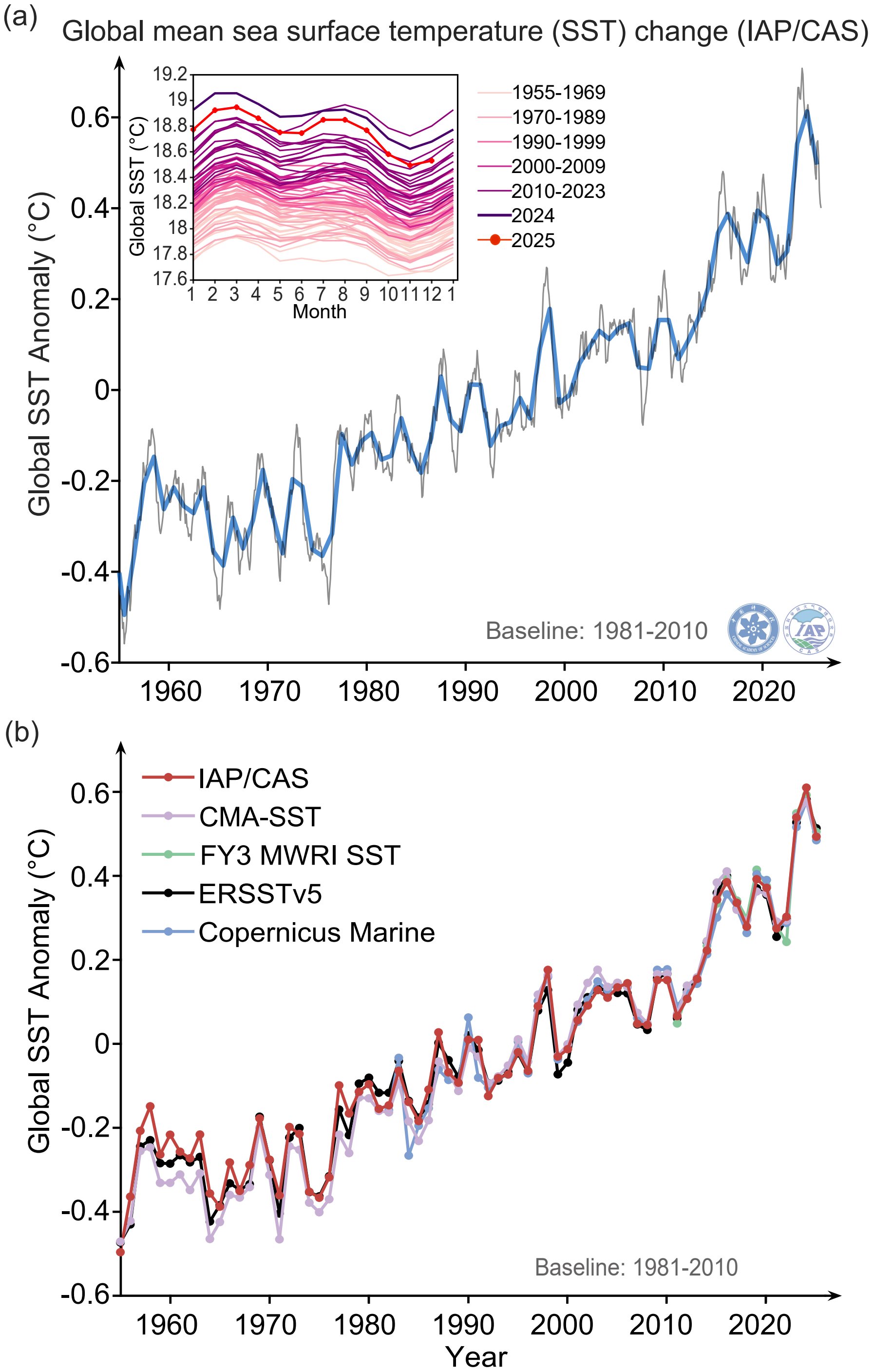

Fig. 4. Global SST changes from 1955 through 2025 (units: °C). (a) The thick lines denote the annual values, and the thin lines represent the monthly values. The SST anomalies are relative to the 1981–2010 baseline. The inset illustrates the intra-annual variability of SST, with 2025 values highlighted in red. (b) Global annual mean SST changes from five data products (ERSST, Copernicus Marine, FY3 MWRI SST, CMA-SST and IAP/CAS). The time series are relative to the 1981–2010 baseline for IAP/CAS, ERSST, Copernicus Marine, and CMA-SST data, whereas FY3 MWRI SST anomalies are relative to the 2011–2025 mean because of the shorter microwave record. To ensure consistency among datasets, the FY3 MWRI SST anomalies are adjusted by subtracting the mean difference between FY3 MWRI SST and IAP/CAS anomalies over their overlapping period (2011–2025).

the strong ENSO fluctuations of previous years (Cheng et al., 2024c, 2025; Pan et al., 2025), as the system re-establishes the west–east thermocline gradient typical of La Niña conditions.

Table 3. Ranked order of the five hottest years of the global mean SST anomaly since 1955 (since 1981 for Copernicus Marine data and since 2011 for MWRI), relative to the 1981–2010 baseline. For FY3 MWRI SST, the SST anomalies are referenced to the IAP baseline because of the shorter record.

Rank	Year	SST anomaly (IAP/CAS) (units: °C)	SST anomaly (ERSST5) (units: °C)	SST anomaly (Copernicus Marine) (units: °C)	SST anomaly (MWRI) (units: °C)	SST anomaly (CMA) (units: °C)
1	2024	0.61	0.58	0.58	0.59	0.58
2	2023	0.54	0.53	0.52	0.55	0.54
3	2025	0.49	0.50	0.49	0.51	0.50
4	2019	0.39	0.37	0.40	0.42	0.36
5	2016	0.39	0.40	0.36	0.40	0.41

(a) 2025 OHC (0-2000 m) anomaly relative to 1981-2010 baseline (IAP/CAS)

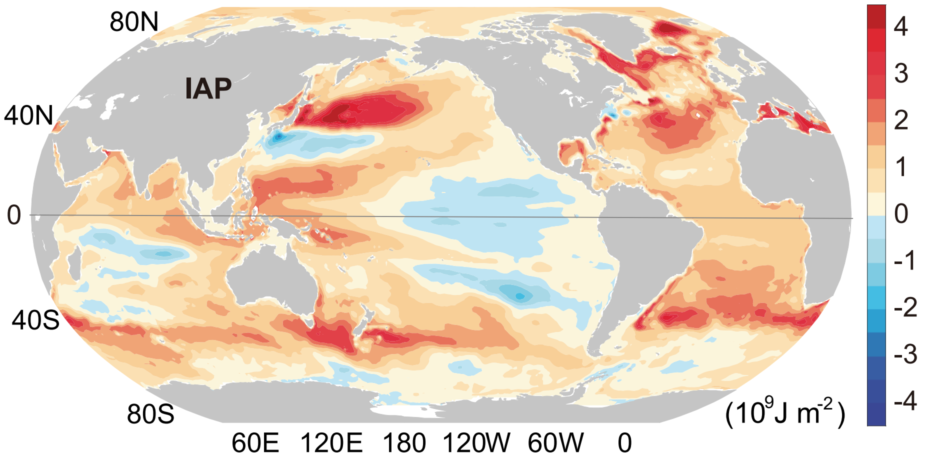

(b) Zonal mean temperature anonamly relative to 1981-2010 baseline (IAP/CAS)

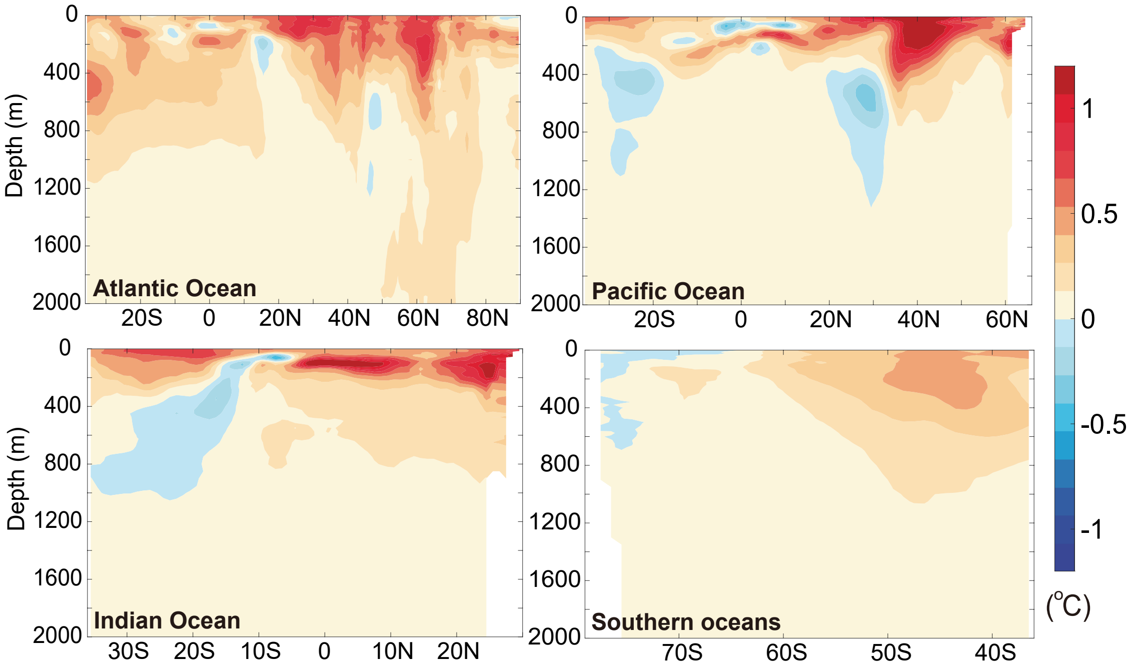

Fig. 5. (a) Annual upper 2000 m OHC anomaly for the global ocean (units: 10^9 J m^{-2}) and (b) zonal-mean temperature anomalies for four major basins (units: °C) in 2025 relative to a 1981–2010 baseline for the IAP/CAS data [data updated from Cheng et al. (2024a)].

Furthermore, the vertical structure of ocean temperature anomalies in 2025 relative to the 1981–2010 climatology is illustrated in Fig. 5b. In all four major basins, positive temperature anomalies are strongest in the upper ~500 m. In the Atlantic Ocean and the Southern Ocean, positive temperature anomalies extend from the surface to at least 2000 m across most latitudes. In the Pacific Ocean, localized subsurface cooling anomalies are pronounced, with the strongest cold signals located near 500 m around 30°N (minimum <–0.3°C) and near 400 m around 25°S (minimum < –0.2°C). In the Indian Ocean, subsurface cooling near the equator extends locally southward and downward, reaching approximately 1000 m south of 30°S, and its underlying processes are discussed in detail later in this section. Together, these basin-scale vertical temperature structures, when integrated over depth, give rise to the observed upper 2000 m OHC anomaly patterns in 2025 (Fig. 5a).

Beyond the anomaly patterns, the spatial distribution of the 2025 upper 2000 m OHC ranking relative to all years since 1958 further reveals how long-term ocean warming and climate variability manifest differently across the global ocean (Fig. 6). Approximately 14% of the global ocean area reached its warmest state on record in 2025, and about 33% fell within its historical top three (57% fell within top five), underscoring the pervasive and accumulated nature of ocean heat gain. The regions with the highest rankings are concentrated in the Southern Ocean, tropical and South Atlantic Ocean, Mediterranean Sea and North Indian Ocean, reflecting their pronounced multi-decadal warming and sustained upper-ocean heat accumulation. It is important to note that because the OHC ranking reflects each region's position relative to its own historical record, high-ranked areas do not necessarily coincide with the strongest 2025 anomalies relative to the 1981–2010 baseline (Fig. 6). Instead, the ranking pattern integrates both long-term heat accumulation and year-to-year variability, revealing where sustained warming has pushed regional conditions to their historical maxima.

Large portions of the subtropical South Indian Ocean and the central equatorial Pacific exhibit notably low rankings in 2025, with their OHC falling within the colder half of the historical record, consistent with Tan et al. (2025b) in that the long-term warming signal in these two regions is still not significantly exceeding the short-term (internal) variability over the past 60 years. The depressed OHC in the subtropical South Indian Ocean is consistent with enhanced wind-driven ocean circulation and Ekman divergence, which promote the upwelling of cooler subsurface waters, a multi-decadal pattern tied to stronger subtropical gyre circulation (Duan et al., 2023) and intensified Southern Hemisphere westerlies (Qu et al., 2019; Hu et al., 2020; Trenberth et al., 2025). This cooling is also reinforced by the concurrent development of La Niña conditions and a negative Indian Ocean Dipole (IOD), which strengthened the southeasterly trade winds and modified the cross-equatorial circulation, thereby enhancing upwelling in the southwestern Indian Ocean (Xie et al., 2002). In the central equatorial Pacific, the low OHC is associated with the developing La Niña conditions discussed above. These low-ranking regions illustrate how regional circulation dynamics can maintain anomalously low heat content even as the global ocean continues to warm overall.

In the Pacific and Indian Ocean, the upper 2000 m OHC in 2025 compared with 2024 exhibits a basin-scale pattern of a La Niña-like redistribution of heat (Fig. 7). The western tropical Pacific shows pronounced warming, with maximum anomalies exceeding 1.7 GJ m^{-2}, and this warm signal spreads meridionally across roughly 25°S–25°N (Fig. 7). In contrast, the central–eastern Pacific off the equator features broad but weaker cooling, reflecting an enhanced west–east OHC gradient. This spatial pattern is consistent with the 2024 post-El Niño adjustment toward weak La Niña conditions of 2025, during which the Indo-Pacific warm pool gradu-

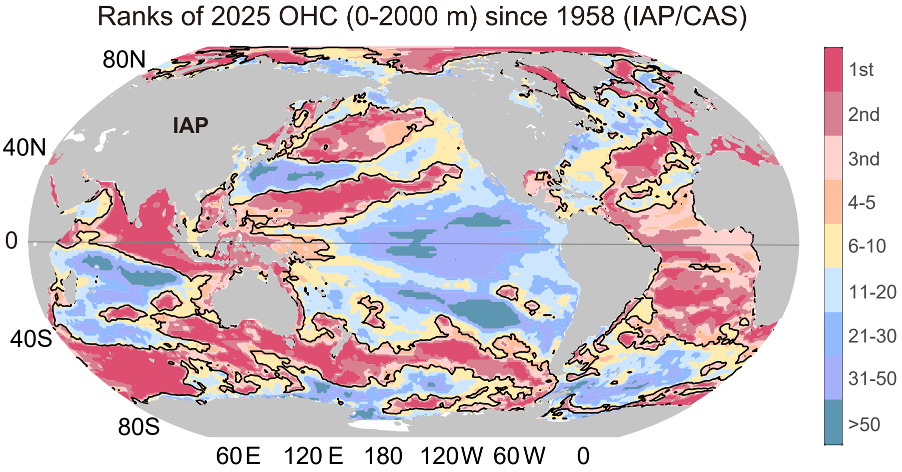

Fig. 6. Global ranking of upper 2000 m OHC in 2025 since 1958 for the IAP/CAS data [data updated from Cheng et al. (2024a)]. The ranking is calculated by sorting the annual 0–2000 m OHC at each grid point from 1958 to 2025, and a rank of 1 indicates the warmest year on record at that location. The black contour lines denote the 5th-warmest year (rank = 5).

(a) 2025 OHC (0-2000 m) anomaly relative to 2024 (IAP/CAS)

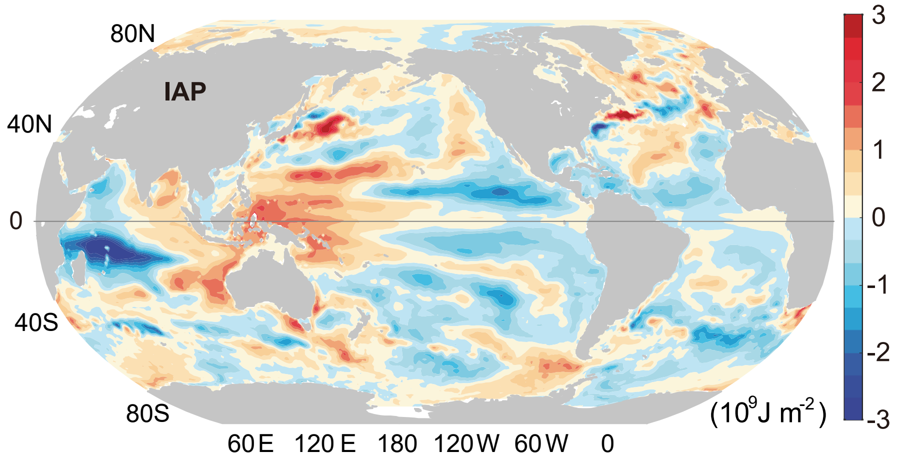

(b) 2025 OHC (0-2000 m) anomaly relative to 2024 (CIGAR-RT)

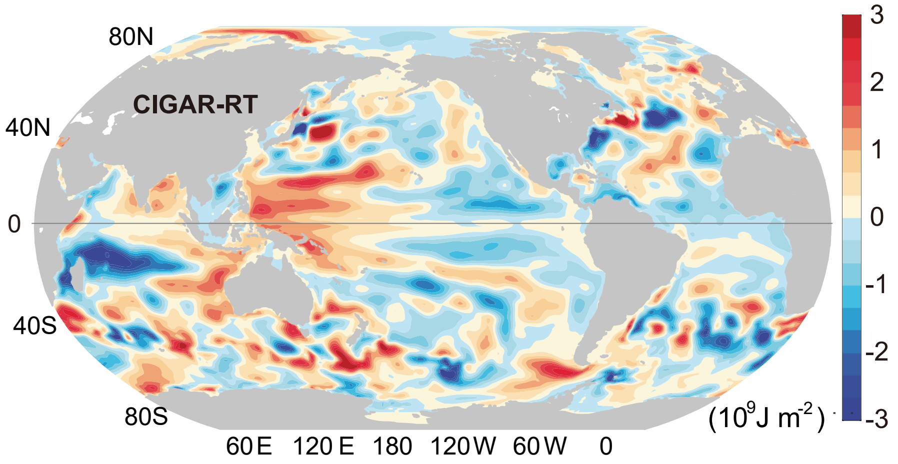

Fig. 7. Differences of annual mean upper 2000 m OHC values between 2025 and 2024, based on (a) IAP/CAS analysis and (b) CIGAR-RT [units: 10^9 J m^{-2}; data updated from Cheng et al. (2024a)].

ally recharges. The increase of OHC in the Indo-Pacific warm pool region is linked to the accumulation of warm water, arising from heat convergence driven by wind stress curl and from the subsurface heat buildup associated with a deepening of the thermocline (England et al., 2014; Latif et al., 2023). At the same time, shoaling of the thermocline in the eastern tropical Pacific enhances the increasing influence of cooler subsurface waters, producing the localized cooling anomalies that accompany the basin's transition toward a re-established west–east thermocline gradient.

The Indian Ocean exhibits a negative IOD pattern, characterized by pronounced cooling in the western basin and warming in the east (Fig. 7). The strong cooling (minimum < −2.8 GJ m^{-2}) in the southwestern Indian Ocean relative to 2024 is consistent with the strengthened southeasterly trade winds and an intensified subtropical gyre, which increase the Ekman divergence and wind-driven upwelling, resulting in the cooling of the upper ocean in this region (Li et al., 2020). In contrast, the eastern Indian Ocean warms in 2025 relative to 2024, consistent with weakened upwelling along the equatorial and Indonesian sectors and reduced entrainment of cooler subsurface waters. Notably, the La Niña-like condition in 2025 also causes warming of the southeast Indian Ocean, with enhanced signatures near the west coast of Australia—a typical response to inter-basin wave propagation (Feng et al., 2013; Li et al., 2017). At the same time, a possibly enhanced inflow of warm western Pacific waters into the Indian Ocean basin, consistent with a strengthened ITF under the prevailing weak La Niña conditions (Mayer et al., 2014) may contribute to the warming of the eastern Indian Ocean. These processes cause a west–east contrast in the southern Indian Ocean OHC change.

5. Spatial patterns of SST changes in 2025

Relative to the 1981–2010 baseline, the 2025 global SST pattern reflects the combined influence of long-term anthropogenic warming and the transition from the strong 2023–2024 El Niño toward ENSO-neutral and developing La Niña conditions (Fig. 8). The most pronounced warm

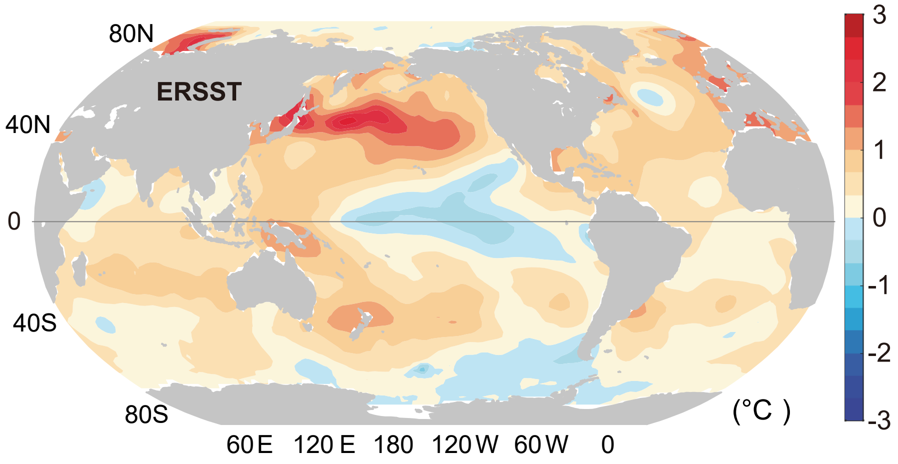

(a) 2025 SST anomaly relative to 1981-2010 baseline (ERSST)

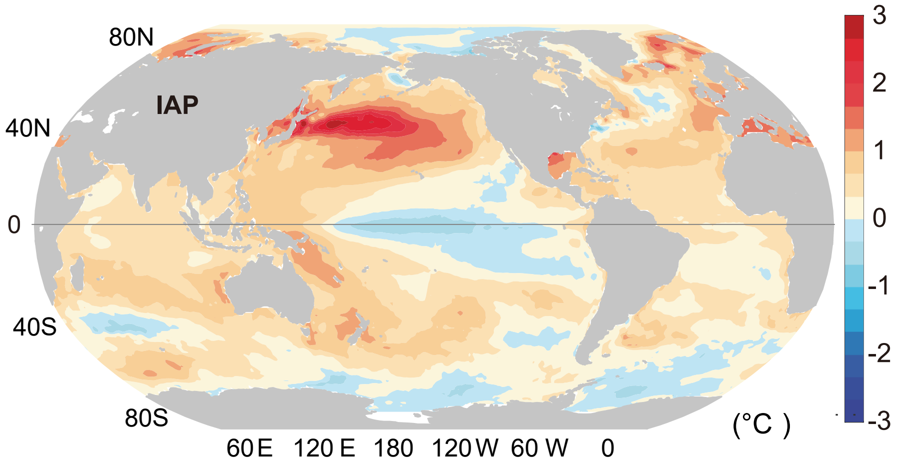

(b) 2025 SST anomaly relative to 1981-2010 baseline (IAP/CAS)

Fig. 8. The annual SST anomaly in 2025 relative to a 1981–2010 baseline for (a) ERSST and (b) IAP/CAS data, separately. Units: °C.

anomalies occur in the northwestern Pacific around 40°N, where SST anomalies exceed 3.0°C, reflecting the enhanced extratropical ocean heat uptake and wind-driven heat convergence that preferentially amplify warming in this latitudinal band (Trenberth et al., 2025). Additional large warm anomalies are found across the broader western North Atlantic and the Mediterranean Sea (maximum > +1.5°C). Widespread warming is also evident throughout much of the Atlantic and Indian Oceans. In contrast, prominent cold anomalies appear in the central and eastern equatorial Pacific, consistent with the basin's transition toward La Niña conditions. Additional weak-to-moderate cooling is observed in sectors adjacent to the Antarctic continent, where freshwater input from ice melt and sea-ice redistribution help maintain suppressed SSTs (Simpkins, 2024).

Compared with 2024, the global SST pattern in 2025 exhibits a widespread and pronounced cooling, particularly across the tropical oceans and the midlatitudes of the ocean in the Northern Hemisphere (Fig. 9). In the Pacific Ocean, a broad cold anomaly emerges across the central and eastern tropical basin, with maximum cooling exceeding 1.2°C and extending meridionally to roughly 20°S–20°N. Substantial cooling is also evident in the Northwest Pacific Ocean, including the region east of China, the Kuroshio and its extension, where SST decreases exceed 2.5°C. This cooling indicates that the warm anomalies that dominated the Northwest Pacific during 2023 and 2024 have begun to diminish (Cheng et al., 2024b, 2025).

The tropical and subtropical Pacific cooling reflects the ongoing transition of the tropical Pacific toward La Niña conditions in 2025. During this transition, the thermocline shoals back toward its climatological depth and the easterly trade winds strengthen, enhancing equatorial upwelling. These processes promote the entrainment of cooler subsurface water into the surface layer, contributing to the widespread cooling across the central and eastern tropical Pacific. In contrast, a pronounced warm anomaly band appears between 20°S and 40°S in the South Pacific Ocean, with warming reaching approximately 1.0°C (Fig. 9). This regional warming is likely associated with an enhanced Hadley circulation, whose strengthened subtropical descent reduces cloud cover, increases shortwave radiation, and suppresses evapora-

(a) 2025 SST anomaly relative to 2024 (ERSST)

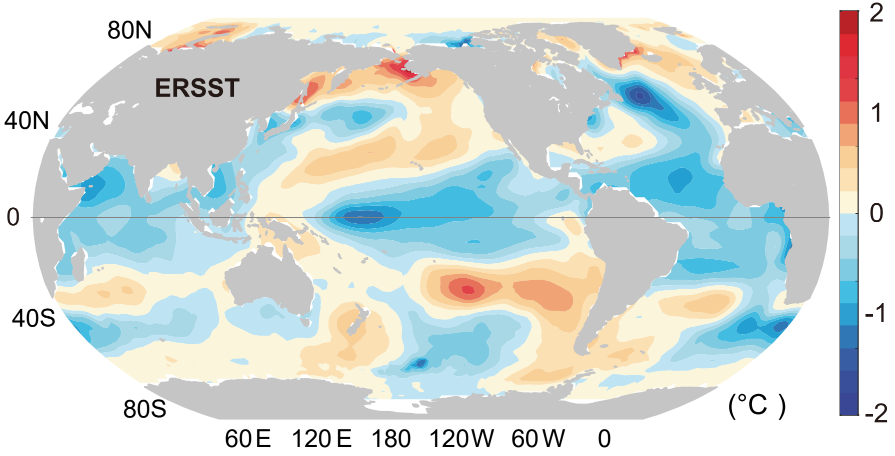

(b) 2025 SST anomaly relative to 2024 (IAP/CAS)

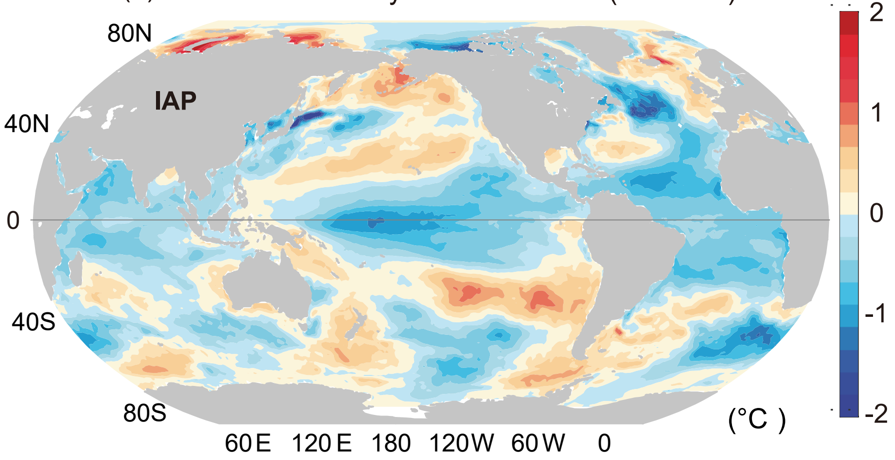

Fig. 9. (a) Differences of annual mean upper SST values between 2025 and 2024, based on (a) ERSST and (b) IAP/CAS analysis. Units: °C.

tive cooling (Oort and Yienger, 1996; Cheng et al., 2019).

The Indian Ocean also shows a cooling from 2024 to 2025 (Fig. 9). North of 20°S, widespread cooling of up to ~0.7°C is evident, while the southern Indian Ocean between 20°S and 40°S exhibits moderate warming of up to ~0.5°C. These patterns are consistent with adjustments in the Hadley and Walker circulations relative to a transition from El Nino to La Niña condition (Cheng et al., 2019; Cai et al., 2021).

In the Atlantic Ocean, a pronounced cooling pattern extends from ~30°S to 55°N, with the strongest anomalies exceeding −1.9°C in the north tropical and subtropical North Atlantic (Fig. 9). In contrast, positive SST anomalies are evident in the eastern midlatitude Atlantic and in the far northern basin north of 55°N, where warming reaches up to +1.3°C.

The Southern Ocean is likewise characterized by a heterogeneous pattern, with widespread warming particularly along the continental margins, where SST anomalies reach as high as +0.9°C (Fig. 9). However, notable cold anomalies appear in several sectors, including regions south of Africa, southwest of Australia, and portions of the South Pacific sector of the Southern Ocean, with minimum values approaching −1.3°C.

6. Regional OHC changes in 2025

Regional variations of upper 2000 m OHC highlight the combined impacts of both anthropogenic-forced long-term changes and prominent interannual-to-decadal variability (Fig. 10). Three out of the eight ocean regions investigated in Fig. 10, including the Southern Oceans, North Atlantic and Mediterranean Sea, show record-high OHC values in 2025.

The Southern Ocean continues its long-term warming since 1958 and exhibits the second strongest OHC increase among all eight regions in 2025 (Fig. 10g). Upper 2000 m OHC increased by 0.11 GJ m^{-2} (10 ZJ) relative to 2024, more than four times the mean heating rate of the past two decades (0.04 GJ m^{-2} yr^{-1} during 2004–2024). Nearly half of the Southern Ocean area reached its historical maximum in 2025 (Fig. 6). This pronounced warming reflects the Southern Ocean's unique role as a major sink of anthropogenic heat, facilitated by strong westerly winds, vigorous

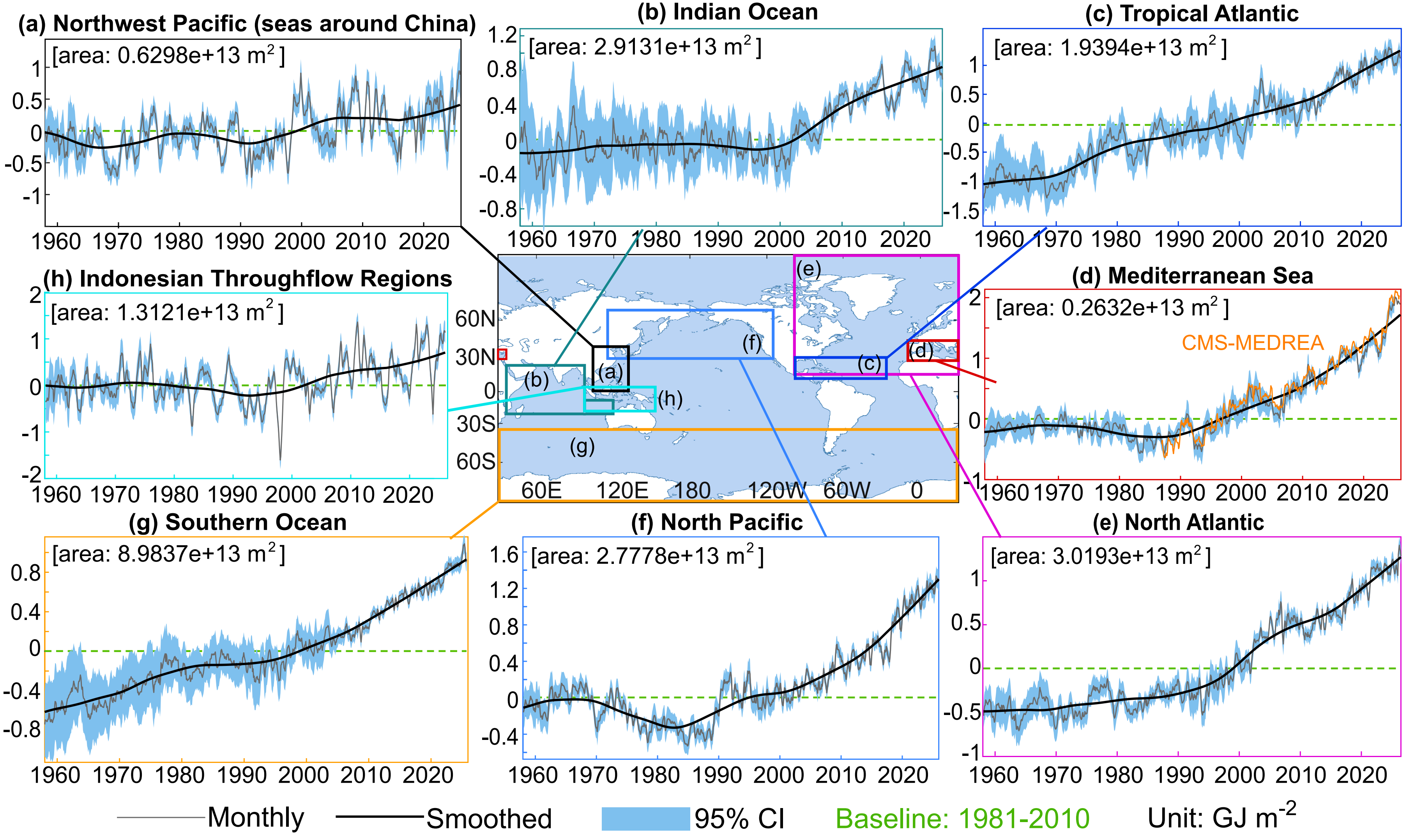

Fig. 10. Regional observed upper 2000 m OHC change from 1958 through 2025 relative to a 1981–2010 baseline using IAP/CAS data (units: ZJ). The time series (black lines) are smoothed by LOWESS with a span width of 240 months. The gray shaded areas are the 95% confidence intervals [data updated from Cheng et al. (2024a)]. For the Mediterranean Sea, an independent OHC estimate from CMS-MEDREA (Escudier et al., 2020, 2021) is shown in panel (d). Note that the y-axis scales differ among panels.

Ekman transport, and deep-reaching overturning circulation that efficiently subduct and store heat below the surface (Armour et al., 2016). Once subducted, the warming signal propagates northward along isopycnal surfaces, affecting the warming in the intermediate and deep water in the Southern Hemisphere (Li et al., 2023; Johnson and Purkey, 2024).

The North Atlantic also warmed notably, with its upper 2000 m OHC in 2025 exceeding that of 2024 by 0.09 GJ m^{-2} (2.7 ZJ), which is slightly larger than its long-term trends (0.04 GJ m^{-2} yr^{-1}) during 2004–2024 (Fig. 10e). These above-trend increments are likely linked to enhanced upper-ocean stratification, which reduces winter mixing and promotes the accumulation of heat within the upper layers (Cheng et al., 2025).

The Mediterranean Sea warms by 0.11 GJ m^{-2} (0.28 ZJ) in 2025 relative to 2024, and this increase also exceeds the long-term trend of 0.07 GJ m^{-2} yr^{-1} observed during 2004–2024 (Fig. 10d). Consistent with this rise, updated measurements along the MX04 Genoa–Palermo transect of the SOOP network (Simoncelli et al., 2024, 2025) indicate continued warming of the intermediate waters (Fig. 11a, b). Intermediate waters form in the eastern Mediterranean and spread towards the western Mediterranean passing through the Sicily Channel (depth: 500 m) where they are monitored by the CNR-ISMAR mooring (red triangle in Fig. 11a) at 400 m deep (Schroeder et al., 2017; Ben Ismail et al., 2021; Cheng et al., 2024b) and flow towards the Tyrrhenian Sea (Pinardi et al., 2015; Von Schuckmann et al., 2016; Simoncelli et al., 2018). Figure 11c shows the monthly temperature obtained from the Sicily Channel mooring measurements (not available after October 2022) at 400 m, the XBT measurements in the layer 200–500 m, and the CMS-MEDREA data along the transect between Tunisia and Sicily averaged below the depth of 200 m (blue line in Fig. 11c). Both the XBT observations and CMS-MEDREA data show sustained temperature increases through 2025, with values reaching the highest levels on record. The coherent warming of these intermediate layers highlights the ongoing heat accumulation within the western Mediterranean.

The OHC in the ITF region ranks as the second warmest in its observational record. Its area-mean OHC rises by 0.58 GJ m^{-2} (7.5 ZJ) relative to 2024, with the largest year-to-year increase among all eight regions (Fig. 10h). Downwelling Rossby waves generated by the La Niña wind anomalies can penetrate from the western Pacific to the Maritime Continent, enhancing the OHC rise of the ITF region (Jin et al., 2024). The Northwest Pacific experiences a similar OHC subsurface enhancement, with its upper 2000 m OHC increasing by 0.29 GJ m^{-2} (1.8 ZJ) and reaching the fourth-highest value since 1958 (Fig. 10a). In both regions, OHC increases are dominated by subsurface warming while SSTs decline in 2025 (Fig. 9), indicating a redistribution of heat within the upper ocean likely linked to strengthened easterly winds, a deepened thermocline, and continued heat accu-

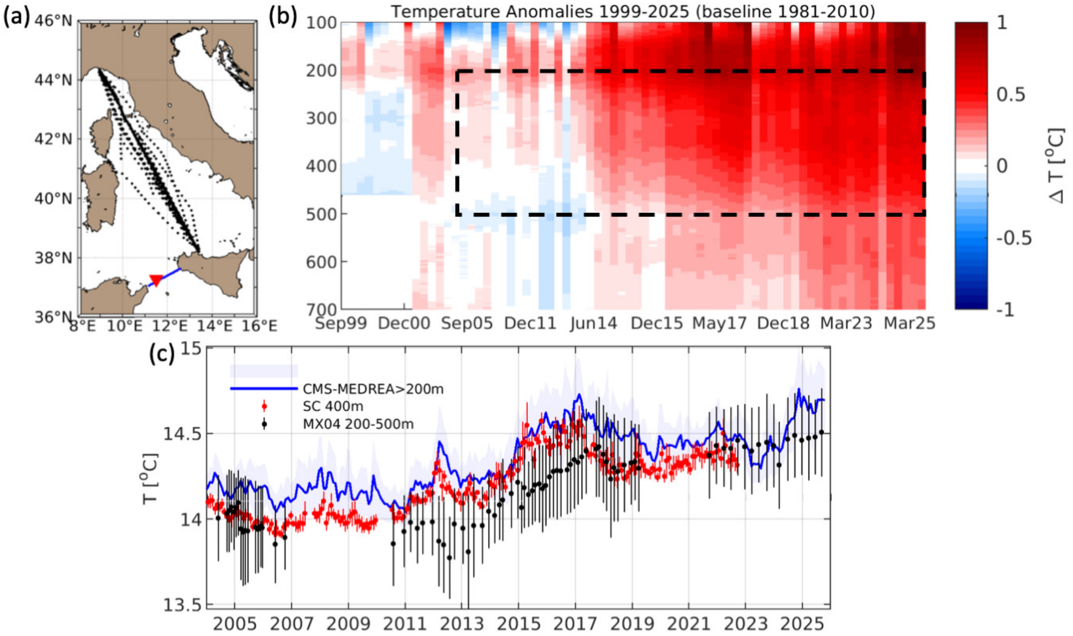

Fig. 11. (a) XBT tracks (black dotted lines) along the MX04 Genova–Palermo transect in the Tyrrhenian and Ligurian seas: the Sicily Channel mooring location (red triangle) and the transect (blue line) used to obtain the CMS-MEDREA (Escudier et al., 2020, 2021) monthly values in (c). (b) Hovmöller plot of mean MX04 temperature anomalies in 1999–2025, computed relative to the 1981–2010 IAP/CAS baseline. (c) MX04 mean temperature values in the 200–500 m layer, monthly mean temperature values at 400 m from the Sicily Channel mooring between 2004 and 2022, and CMS-MEDREA estimates below 200 m. The blue shading represents the uncertainty of the CMS-MEDREA reanalysis below 200m. The black error bars represent the standard deviation of temperature values between 200 and 500 m derived from all XBT profiles collected during each cruise, while the red error bars indicate the standard deviation of temperature values recorded at a single location and fixed depth.

mulation in the Indo-Pacific warm pool.

For the North Pacific, the annual OHC in 2025 remains nearly unchanged relative to 2024, ranking as the second highest since 1958 (Fig. 10f). However, the tropical Atlantic exhibits a modest decrease, with a basin-mean reduction of approximately −0.10 GJ m^{-2} (−1.9 ZJ), still placing 2025 as its fourth warmest year on record (Fig. 10c). In contrast, the Indian Ocean experiences the strongest cooling among eight regions, with its upper 2000 m OHC decreasing by 0.22 GJ m^{-2} (6.5 ZJ) relative to 2024, largely driven by the pronounced cold anomalies in the west Indian Ocean (Fig. 7, 10b). Nevertheless, the annual basin's OHC in 2025 still ranks as the third highest in the historical record, reflecting the dominant role of long-term anthropogenic warming that persists even during years of regional cooling.

7. Concluding remarks

This study provides updated assessments of global SST and upper OHC for the year 2025 based on multiple observational and reanalysis datasets produced by independent research groups. The results show that the global ocean continued to warm in 2025, with the upper 2000 m OHC reaching the highest value ever observed, despite a prevailing weak La Niña state throughout the year. According to IAP/CAS estimates, the global ocean gained approximately 23 ZJ of heat relative to 2024, with about 33% of the global ocean area reaching the top three warmest values in their historical records. Three additional products, CIGAR-RT, NCEI/NOAA and Copernicus Marine, independently confirm substantial OHC increases, highlighting the robustness of the 2025 warming signal.

In addition to setting a new record in 2025, the global ocean continues to show sustained and intensified warming. All four OHC products reveal a persistent increase in the ocean heating rate, especially evident in recent decades, and further supported by CERES EEI. Such ocean warming can amplify climate impacts, contributing to faster sea-level rise, a stronger hydrological cycle, and more frequent and intense marine heatwaves.

Further, spatial and regional differences are evident in the upper OHC distribution. Strong warming occurred in the Southern Ocean, North Atlantic, Mediterranean Sea, and warm pool of the Indo-Pacific, while cooling emerged in the equatorial Pacific, the western Indian Ocean, and the tropical Atlantic, partly reflecting basin-scale dynamical adjustments associated largely with a transition to La Niña conditions. The North Atlantic and the Mediterranean Sea are also the climate hotspots of salinization, deoxygenation, and acidification, and therefore the concurrent change (e.g., double and triple changes) of the above four climatic impact drivers (temperature, salinity, dissolved oxygen, and pH) indicates a deep-reaching compound ocean state change in the North Atlantic and the Mediterranean Sea, making the ocean ecosystems and the life they support more fragile (Tan et al., 2025b).

In contrast to the OHC increase, the global mean SST cooled slightly by about 0.08~0.12°C relative to 2024, though it still ranked as the third-warmest year on record and remained far above the 1981–2010 climatological baseline. This surface cooling is consistent with the ocean state transition from the strong 2023–24 El Niño to La Niña conditions, accompanied by widespread cooling in the tropical oceans and midlatitude Northern Hemisphere.

Ocean warming continues to exert profound impacts on the Earth system. Rising OHC remains the fundamental contributor to global sea-level rise via thermal expansion, reinforces marine heatwaves, and intensifies extreme weather events by increasing heat and moisture exchanges with the atmosphere. In the long term, consistent with projections from state-of-the-art climate models, global OHC is expected to continue breaking records until net-zero greenhouse gas emissions are achieved, given the persistence of a positive EEI. Sustained and accurate monitoring of both EEI and OHC is essential for detecting changes in the pace of climate warming and for constraining the global energy budget, with recent studies also exploring emerging physically informed data-driven approaches as complementary tools for short-term prediction and gap-filling of ocean environmental variables (e.g., Cheng et al., 2022a, c; Liu et al., 2025). At the same time, the continuity of space-based observations remains fragile, underscoring the risk of losing critical information on the planet's energy flows (Mauritsen et al., 2025). Strengthening the ocean observing system and advancing mechanistic understanding of ocean heat redistribution are therefore essential for improving climate assessments, supporting adaptation planning, and informing sustainable and climate-resilient development pathways.

Acknowledgments. The IAP/CAS analysis is supported by the National Key R&D Program of China (Grant No. 2023YFF0806500), the International Partnership Program of the Chinese Academy of Sciences (Grant No. 060GJHZ2024064MI), the Chinese Academy of Sciences and the National Research Council of Italy Scientific Cooperative Programme, the new Cornerstone Science Foundation through the XPLORER PRIZE, the National Key Scientific and Technological Infrastructure project "Earth System Science Numerical Simulator Facility" (EarthLab), and Ocean Negative Carbon Emissions (ONCE). The numerical calculations in this study were carried out by eODS (an easy-to-use Ocean observation Data processing Software package, jointly developed by CNIC and IAP) on the ORISE Supercomputer. NCAR is sponsored by the US National Science Foundation. G. LI is supported by the Young Talent Support Project of Guangzhou Association for Science and Technology and the Natural Science Foundation of China (Grant number 42206208). We integrated some data collected onboard R/V Shiyan 6 implementing the Open Research Cruise NORC2022-10+NORC2022-303 supported by NSFC shiptime Sharing Projects 42149910. We acknowledge the Earthlink tool(https://github.com/OpenEarthLab/EarthLink) for providing insights into the analysis of some results in this study. The efforts of Dr. Fasullo in this work were supported by NASA Awards 80NSSC21K1191, 80NSSC17K0565, and 80NSSC22K0046, and portions of this study were supported by the Regional and Global Model Analysis (RGMA) component of the Earth and Environmental System Modeling Program of the U.S. Department of Energy's Office of Biological & Environmental Research (BER) under the Lawrence Livermore National Lab subaward DE-AC52-07NA27344, Lawrence Berkeley National Lab subaward DE-AC02-05CH11231, and Pacific Northwest National Lab subaward DE-AC05-76RL01830. This work was also supported by the National Science Foundation (NSF) National Center for Atmospheric Research, under Cooperative Agreement No. 1852977. The efforts of Dr. Mishonov were supported by NOAA (Grant No. NA19NES4320002 and NA24NESX432C0001 to CISESS-MD at the University of Maryland). The efforts of Dr. Mayer were supported by the European Space Agency (ESA) under contract 4000145298/24/I-LR (MOTECUSOMA) and contract 4000147586/I/25-LR (CCI Ocean Surface Heat Fluxes). The CNR-ISMAR CIGAR reanalysis is supported by the Copernicus Marine Service (contract 24254L01-COP-GLORAN GREP-4000). From 2021 to 2024, the XBT data have been collected under the framework of the MACMAP project funded by the Istituto Nazionale di Geofisica e Vulcanologia (INGV) in agreement between INGV, ENEA, and GNV SpA shipping company, which provides hospitality on its commercial vessels. From December 2024, the XBT monitoring is supported by INGV funds.

Data availability. The IAP/CAS data are available at http://www.ocean.iap.ac.cn/, https://msdc.qdio.ac.cn/, and https://doi.org/10.57760/sciencedb.35026. The WOD is available at https://www.ncei.noaa.gov/products/world-ocean-database. The NCEI/NOAA data are available at https://www.ncei.noaa.gov/products/climate-data-records/global-ocean-heat-content. The Post-quality-controlled Argo data are from the China Argo Real-time Data Center (https://www.argo.org.cn/). This study was conducted by also using E.U. Copernicus Marine Service Information (https://marine.copernicus.eu/) for the Mediterranean OHC estimates (https://doi.org/10.25423/CMCC/MEDSEA_MULTIYEAR_PHY_006_004_E3R1). The Copernicus Marine OHC data are from https://data.marine.copernicus.eu/product/INSITU_GLO_PHY_TS_OA_NRT_013_002/description (EU Copernicus Marine Service Product, 2023a). The OSTIA data are from https://data.marine.copernicus.eu/product/SST_GLO_SST_L4_REP_OBSERVATIONS_010_011/description (EU Copernicus Marine Service Product, 2023b, 2023c). The CO_2 data are from https://gml.noaa.gov/ccgg/trends/. The FY3 MWRI SST data are from http://data.nsmc.org.cn/DataPortal/cn/theme/detail.html?doi=10.12185/NSMC.REPROC.RPD.SST.FY3.MWRI.L3.GBAL.POAM.GLL.025KM.HDF.2024.33.V1&id=148. The CMA-SST data are from http://218.91.114.36:9903/entest/#/Visualization/Visualization-detail?id=16. The GMST data from Berkeley Earth are available at https://berkeleyearth.org/june-2024-temperature-update/. The Antarctic sea-ice information is from https://nsidc.org/sea-ice-today/analyses/antarctic-sea-ice-maximum-settles-third-place. The Arctic sea-ice information is from https://nsidc.org/sea-ice-today/analyses/2025-arctic-sea-ice-minimum-squeezes-ten-lowest-minimums. XBT data are accessible through ERDDAP at https://oceano.bo.ingv.it/erddap/index.html. Paris Agreement texts can be found at https://www.un.org/en/climatechange/paris-agreement. The CIGAR reanalysis is described at http://cigar.ismar.cnr.it, where there are links for data download, while the entire dataset is accessible via ftp upon request; the reanalysis uses data from ERA5 (https://cds.climate.copernicus.eu/datasets/reanalysis-era5-single-levels), UKMO EN4.2.2(https://www.metoffice.gov.uk/hadobs/en4/download-en4-2-2.html), JRA-55-do (https://climate.mri-jma.go.jp/pub/ocean/JRA55-do), COBEv2 SST (https://psl.noaa.gov/data/gridded/data.cobe2.html), HadISST SST (https://www.metoffice.gov.uk/hadobs/hadisst), and Argo data from the Coriolis/Ifremer GDAC (https://data-argo.ifremer.fr) (Argo, 2023). The NEMO model is available from https://www.nemo-ocean.eu with modifications contained in the CNR-ISMAR repository (https://baltig.cnr.it/nemo_ismar-rm/nemo_4.0.7/-/tree/3.0?ref_type=tags). CERES data are available from https://ceres.larc.nasa.gov/data/.

REFERENCES

Ablain, M. and Coauthors: Uncertainty in satellite estimates of global mean sea-level changes, trend and acceleration. *Earth System Science Data*, **11**, 1189−1202, 2019, https://doi.org/10.5194/essd-11-1189-2019.

Allan, R. P., 2023: Amplified seasonal range in precipitation minus evaporation. *Environmental Research Letters*, **18**, 094004, https://doi.org/10.1088/1748-9326/acea36.

Argo, 2023: Argo Float Data and Metadata from Global Data Assembly Centre (Argo GDAC). SEANOE. Available from https://doi.org/10.17882/42182.

Armour, K. C., J. Marshall, J. R. Scott, A. Donohoe, and E. R. Newsom, 2016: Southern Ocean warming delayed by circumpolar upwelling and equatorward transport. *Nature Geoscience*, **9**, 549−554, https://doi.org/10.1038/ngeo2731.

Ben Ismail S., K. Schroeder, J. Chiggiato, S. Sparnocchia, and M. Borghini, 2021: Long term changes monitored in two Mediterranean Channels. *Copernicus Marine Service Ocean State Report, Issue 5*, K. Von Schuckmann et al., Eds., 48−52, https://doi.org/10.1080/1755876X.2021.1946240.

Blunden, J., J. Reagan, and R. J. H. Dunn, 2025: State of the climate in 2024. *Bull. Amer. Meteor. Soc.*, **106**, S1−S513, https://doi.org/10.1175/2025BAMSStateoftheClimate.1.

Boyer, T. P., and Coauthors, 2018: World Ocean Database 2018. A.V. Mishonov, Technical Ed., NOAA Atlas NESDIS 87.

Brett, L., C. J. White, D. I. V. Domeisen, B. van den Hurk, P. Ward, and J. Zscheischler, 2025: Review article: The growth in compound weather and climate event research in the decade since SREX. *Natural Hazards and Earth System Sci-*

ences, **25**, 2591–2611, https://doi.org/10.5194/nhess-25-2591-2025.

Cai, W. J., and Coauthors, 2021: Changing El Niño–Southern Oscillation in a warming climate. *Nature Reviews Earth & Environment*, **2**, 628–644, https://doi.org/10.1038/s43017-021-00199-z.

Capotondi, A., and Coauthors, 2024: A global overview of marine heatwaves in a changing climate. *Communications Earth & Environment*, **5**, 701, https://doi.org/10.1038/s43247-024-01806-9.

Chen, L. F., L. J. Cao, Z. J. Zhou, D. B. Zhang, and J. Liao, 2021: A new globally reconstructed sea surface temperature analysis dataset since 1900. *J. Meteor. Res.*, **35**, 911–925, https://doi.org/10.1007/s13351-021-1098-7.

Chen, L. F., W. H. Xu, Z. J. Zhou, L. J. Cao, S. Yang, and C. D. Xu, 2025: A new global land–ocean merged surface temperature dataset since the 1850s: The CMA-GMST dataset. *Climate Dyn.*, **63**, 187, https://doi.org/10.1007/s00382-025-07614-x.

Cheng, L. J., J. Abraham, Z. Hausfather, and K. E. Trenberth, 2019: How fast are the oceans warming?. *Science*, **363**, 128–129, https://doi.org/10.1126/science.aav7619.

Cheng, L. J., G. Foster, Z. Hausfather, K. E. Trenberth, and J. Abraham, 2022b: Improved quantification of the rate of ocean warming. *J. Climate*, **35**, 4827–4840, https://doi.org/10.1175/JCLI-D-21-0895.1.

Cheng, L. J., K. E. Trenberth, J. Fasullo, T. Boyer, J. Abraham, and J. Zhu, 2017a: Improved estimates of ocean heat content from 1960 to 2015. *Science Advances*, **3**, e1601545, https://doi.org/10.1126/sciadv.1601545.

Cheng, L. J., K. Trenberth, J. Fasullo, J. Abraham, T. Boyer, K. Von Schuckmann, and J. Zhu, 2017b: Taking the pulse of the planet. *EOS, Transactions American Geophysical Union*, **98**, 14–15, https://doi.org/10.1029/2017EO081839.

Cheng, L. J., K. von Schuckmann, A. Minière, M. Z. Hakuba, S. Purkey, G. A. Schmidt, and Y. Pan, 2024c: Ocean heat content in 2023. *Nature Reviews Earth & Environment*, **5**, 232–234, https://doi.org/10.1038/s43017-024-00539-9.

Cheng, L. J., and Coauthors, 2022a: Past and future ocean warming. *Nature Reviews Earth & Environment*, **3**, 776–794, https://doi.org/10.1038/s43017-022-00345-1.

Cheng, L. J., and Coauthors, 2022c: Another record: Ocean warming continues through 2021 despite La Niña conditions. *Adv. Atmos. Sci.*, **39**, 373–385, https://doi.org/10.1007/s00376-022-1461-3.

Cheng, L. J., and Coauthors, 2024a: IAPv4 ocean temperature and ocean heat content gridded dataset. *Earth System Science Data*, **16**, 3517–3546, https://doi.org/10.5194/essd-16-3517-2024.

Cheng, L. J., and Coauthors, 2024b: New record ocean temperatures and related climate indicators in 2023. *Adv. Atmos. Sci.*, **41**, 1068–1082, https://doi.org/10.1007/s00376-024-3378-5.

Cheng, L. J., and Coauthors, 2025: Record high temperatures in the ocean in 2024. *Adv. Atmos. Sci.*, **42**, 1092–1109, https://doi.org/10.1007/s00376-025-4541-3.

Cologna, V., and Coauthors, 2025: Extreme weather event attribution predicts climate policy support across the world. *Nature Climate Change*, **15**, 725–735, https://doi.org/10.1038/s41558-025-02372-4.

Copernicus Climate Change Service, 2025: European summer 2025 – hot in the west and south, dry in the southeast. Copernicus Climate Bulletin. Available from https://climate.copernicus.eu/european-summer-2025-hot-west-and-south-dry-southeast.

Dong, T. Y., and Coauthors, 2025: Record-breaking 2023 marine heatwaves. *Science*, **389**, 369–374, https://doi.org/10.1126/science.adr0910.

Duan, J., Y. L. Li, L. J. Cheng, P. F. Lin, and F. Wang, 2023: Heat storage in the upper Indian Ocean: The role of wind-driven redistribution. *J. Climate*, **36**, 2221–2242, https://doi.org/10.1175/JCLI-D-22-0534.1.

England, M. H., and Coauthors, 2014: Recent intensification of wind-driven circulation in the Pacific and the ongoing warming hiatus. *Nature Climate Change*, **4**, 222–227, https://doi.org/10.1038/nclimate2106.

Escudier, R., and Coauthors, 2020: Mediterranean Sea Physics Reanalysis (CMEMS MED-Currents, E3R1 system) (Version 1) [Data set]. Copernicus Monitoring Environment Marine Service (CMEMS), https://doi.org/10.25423/CMCC/MEDSEA_MULTIYEAR_PHY_006_004_E3R1.

Escudier, R., and Coauthors, 2021: A high resolution reanalysis for the Mediterranean Sea. *Frontiers in Earth Science*, **9**, 702285, https://doi.org/10.3389/feart.2021.702285.

EU Copernicus Marine Service Product, 2023a: Global Ocean-Real time in-situ observations objective analysis. Mercator Ocean International [data set], https://doi.org/10.48670/moi-00037.

EU Copernicus Marine Service Product, 2023b: Global Ocean OSTIA Sea Surface Temperature and Sea Ice Reprocessed. Mercator Ocean International [data set], https://doi.org/10.48670/moi-00168.

EU Copernicus Marine Service Product, 2023c: Global Ocean OSTIA Sea Surface Temperature and Sea Ice Analysis. Mercator Ocean International [data set], https://doi.org/10.48670/moi-00165.

Feng, M., M. J. McPhaden, S.-P. Xie, and J. Hafner, 2013: La Niña forces unprecedented Leeuwin Current warming in 2011. *Scientific Reports*, **3**, 1277, https://doi.org/10.1038/srep01277.

Good, S., and Coauthors, 2020: The current configuration of the OSTIA system for operational production of foundation sea surface temperature and ice concentration analyses. *Remote Sensing*, **12**, 720, https://doi.org/10.3390/rs12040720.

Hakuba, M. Z., and Coauthors, 2024: Trends and variability in Earth's energy imbalance and ocean heat uptake since 2005. *Surveys in Geophysics*, **45**, 1721–1756, https://doi.org/10.1007/s10712-024-09849-5.

Hansen, J., M. Sato, P. Kharecha, and K. von Schuckmann, 2011: Earth's energy imbalance and implications. *Atmospheric Chemistry and Physics*, **11**, 13 421–13 449, https://doi.org/10.5194/acp-11-13421-2011.

Hersbach, H., and Coauthors, 2023: ERA5 monthly averaged data on pressure levels from 1940 to present. Copernicus Climate Change Service (C3S) Climate Data Store (CDS), https://doi.org/10.24381/cds.6860a573.

Hu, S. J., J. Sprintall, C. Guan, M. J. McPhaden, F. Wang, D. X. Hu, and W. J. Cai, 2020: Deep-reaching acceleration of global mean ocean circulation over the past two decades. *Science Advances*, **6**, eaax7727, https://doi.org/10.1126/sciadv.aax7727.

Huang, B. Y., and Coauthors, 2017: Extended reconstructed sea surface temperature, Version 5 (ERSSTv5): Upgrades, validations, and intercomparisons. *J. Climate*, **30**, 8179–8205, https://doi.org/10.1175/JCLI-D-16-0836.1.

Huang, B. Y., and Coauthors, 2020: Uncertainty estimates for sea surface temperature and land surface air temperature in NOAAGlobalTemp version 5. *J. Climate*, **33**, 1351–1379, https://doi.org/10.1175/JCLI-D-19-0395.1.

IPCC, 2021: *Climate Change 2021: The Physical Science Basis. Contribution of Working Group I to the Sixth Assessment Report of the Intergovernmental Panel on Climate Change*. Cambridge University Press, https://doi.org/10.1017/9781009157896.

Ishii, M., A. Shouji, S. Sugimoto, and T. Matsumoto, 2005: Objective analyses of sea-surface temperature and marine meteorological variables for the 20th century using ICOADS and the Kobe Collection. *International Journal of Climatology*, **25**, 865–879, https://doi.org/10.1002/joc.1169.

Jin, Y. C., Y. L. Li, L. J. Cheng, J. Duan, R. Li, and F. Wang, 2024: Ocean heat content increase of the Maritime Continent since the 1990s. *Geophys. Res. Lett.*, **51**, e2023GL107526, https://doi.org/10.1029/2023GL107526.

Johnson, G. C., and S. G. Purkey, 2024: Refined estimates of global ocean deep and abyssal decadal warming trends. *Geophys. Res. Lett.*, **51**, e2024GL111229, https://doi.org/10.1029/2024GL111229.

Judd, E. J., J. E. Tierney, D. J. Lunt, I. P. Montañez, B. T. Huber, S. L. Wing, and P. J. Valdes, 2024: A 485-million-year history of Earth's surface temperature. *Science*, **385**, eadk3705, https://doi.org/10.1126/science.adk3705.

Latif, M., and Coauthors, 2023: Strengthening atmospheric circulation and trade winds slowed tropical Pacific surface warming. *Communications Earth & Environment*, **4**, 249, https://doi.org/10.1038/s43247-023-00912-4.

Lenssen, N. J. L., G. A. Schmidt, J. E. Hansen, M. J. Menne, A. Persin, R. Ruedy, and D. Zyss, 2019: Improvements in the GISTEMP uncertainty model. *J. Geophys. Res.: Atmos.*, **124**(12), 6307–6326, https://doi.org/10.1029/2018JD029522.

Levitus, S., and Coauthors, 2012: World ocean heat content and thermosteric sea level change (0–2000 m), 1955–2010. *Geophys. Res. Lett.*, **39**, L10603, https://doi.org/10.1029/2012GL051106.

Li, C. Y., W. Zhou, X. L. Jia, and X. Wang, 2006: Decadal/Interdecadal variations of the ocean temperature and its impacts on climate. *Adv. Atmos. Sci.*, **23**, 964–981, https://doi.org/10.1007/s00376-006-0964-7.

Li, W. H., L. F. Li, M. Ting, and Y. M. Liu, 2012: Intensification of Northern Hemisphere subtropical highs in a warming climate. *Nature Geoscience*, **5**, 830–834, https://doi.org/10.1038/ngeo1590.

Li, Y. L., W. Q. Han, and L. Zhang, 2017: Enhanced decadal warming of the southeast Indian Ocean during the recent global surface warming slowdown. *Geophys. Res. Lett.*, **44**, 9876–9884, https://doi.org/10.1002/2017gl075050.

Li, Y. L., W. Q. Han, F. Wang, L. Zhang, and J. Duan, 2020: Vertical structure of the upper Indian Ocean thermal variability. *J. Climate*, **33**, 7233–7253, https://doi.org/10.1175/JCLI-D-19-0851.1.

Li, Z., M. H. England, and S. Groeskamp, 2023: Recent acceleration in global ocean heat accumulation by mode and intermediate waters. *Nature Communications*, **14**, 6888, https://doi.org/10.1038/s41467-023-42468-z.

Liu, Z., Z. Li, S. Lu, X. Wu, C. Sun, and J. Xu, 2021: Scattered Dataset of Global Ocean Temperature and Salinity Profiles from the International Argo Program. *Journal of Global Change Data & Discovery*, **5**, 22–31, https://doi.org/10.3974/geodp.2021.04.03.

Liu, Q. H., S. L. Bao, H. Q. Yan, H. Z. Wang, Y. J. Wang, and R. Zhang, 2025: Enhancing sea surface salinity short-term prediction using physically informed deep learning. *Applied Ocean Research*, **165**, 104832, https://doi.org/10.1016/j.apor.2025.104832.

Loeb, N. G., and Coauthors, 2018: Clouds and the Earth's Radiant Energy System (CERES) Energy Balanced and Filled (EBAF) Top-of-Atmosphere (TOA) Edition-4.0 Data Product. *J. Climate*, **31**, 895–918, https://doi.org/10.1175/JCLI-D-17-0208.1.

Loeb, N. G., G. C. Johnson, T. J. Thorsen, J. M. Lyman, F. G. Rose, and S. Kato, 2021: Satellite and ocean data reveal marked increase in Earth's heating rate. *Geophys. Res. Lett.*, **48**, e2021GL093047, https://doi.org/10.1029/2021GL093047.

Loeb, N. G., and Coauthors, 2022: Evaluating twenty-year trends in Earth's energy flows from observations and reanalyses. *J. Geophys. Res.: Atmos.*, **127**, e2022JD036686, https://doi.org/10.1029/2022JD036686.

Ma, J., and Coauthors, 2020: Hydrological cycle changes under global warming and their effects on multiscale climate variability. *Annals of the New York Academy of Sciences*, **1472**, 21–48, https://doi.org/10.1111/nyas.14335.

Marcos, M., A. Amores, M. Agulles, J. Robson, and X. B. Feng, 2025: Global warming drives a threefold increase in persistence and 1°C rise in intensity of marine heatwaves. *Proceedings of the National Academy of Sciences of the United States of America*, **122**, e2413505122, https://doi.org/10.1073/pnas.2413505122.

Mauritsen, T., and Coauthors, 2025: Earth's energy imbalance more than doubled in recent decades. *AGU Advances*, **6**, e2024AV001636, https://doi.org/10.1029/2024AV001636.

Mayer, M., L. Haimberger, and M. A. Balmaseda, 2014: On the energy exchange between tropical ocean basins related to ENSO. *J. Climate*, **27**, 6393–6403, https://doi.org/10.1175/JCLI-D-14-00123.1.

Mayer, J., M. Mayer, L. Haimberger, and C. Liu, 2022: Comparison of surface energy fluxes from global to local scale. *J. Climate*, **35**, 4551–4569, https://doi.org/10.1175/JCLI-D-21-0598.1.

Mayer, M., and Coauthors, 2024: Assessment of atmospheric and surface energy budgets using observation-based data products. *Surv. Geophys.*, **45**, 1827–1854, https://doi.org/10.1007/s10712-024-09827-x.

Minière, A., K. Von Schuckmann, J.-B. Sallée, and L. Vogt, 2023: Robust acceleration of Earth system heating observed over the past six decades. *Scientific Reports*, **13**, 22975, https://doi.org/10.1038/s41598-023-49353-1.

Mishonov, A. V., and Coauthors, 2024: World Ocean Database 2023. NOAA Atlas NESDIS 97, https://doi.org/10.25923/z885-h264.

Morice, C. P., and Coauthors, 2021: An updated assessment of near-surface temperature change from 1850: The HadCRUT 5 data set. *J. Geophys. Res.: Atmos.*, **126**, e2019JD032361, https://doi.org/10.1029/2019JD032361.

Nigam, T., and Coauthors, 2021: Mediterranean Sea Physical Reanalysis INTERIM (CMEMS MED-Currents, E3R1i system) (Version 1) [Data set]. Copernicus Monitoring Environment Marine Service (CMEMS), https://doi.org/10.25423/

cmcc/medsea_multiyear_phy_006_004_e3r1i.

Oort, A. H., and J. J. Yienger, 1996: Observed interannual variability in the Hadley circulation and its connection to ENSO. *J. Climate*, **9**, 2751–2767, https://doi.org/10.1175/1520-0442(1996)009<2751:OIVITH>2.0.CO;2.

Pan, Y. Y., A. Minière, K. von Schuckmann, Z. Li, Y. L. Li, L. J. Cheng, and J. Zhu, 2025: Ocean heat content in 2024. *Nature Reviews Earth & Environment*, **6**, 249–251, https://doi.org/10.1038/s43017-025-00655-0.

Pinardi, N., and Coauthors, 2015: Mediterranean Sea large-scale low-frequency ocean variability and water mass formation rates from 1987 to 2007: A retrospective analysis. *Progress in Oceanography*, **132**, 318–332, https://doi.org/10.1016/j.pocean.2013.11.003.

Qu, T. D., I. Fukumori, and R. A. Fine, 2019: Spin-up of the Southern Hemisphere super gyre. *J. Geophys. Res.: Oceans*, **124**, 154–170, https://doi.org/10.1029/2018jc014391.

Rayner, N. A., D. E. Parker, E. B. Horton, C. K. Folland, L. V. Alexander, D. P. Rowell, E. C. Kent, and A. Kaplan, 2003: Global analyses of sea surface temperature, sea ice, and night marine air temperature since the late nineteenth century. *J. Geophys. Res.: Atmos.*, **108**, 4407, https://doi.org/10.1029/2002JD002670.

Ripple, W. J., and Coauthors, 2025: The 2025 state of the climate report: A planet on the brink. *BioScience*, **75**, 1016–1027, https://doi.org/10.1093/biosci/biaf149.

Rohde, R. A., and Z. Hausfather, 2020: The Berkeley earth land/ocean temperature record. *Earth System Science Data*, **12**, 3469–3479, https://doi.org/10.5194/essd-12-3469-2020.

Schroeder, K., J. Chiggiato, S. A. Josey, M. Borghini, S. Aracri, and S. Sparnocchia, 2017: Rapid response to climate change in a marginal sea. *Scientific Reports*, **7**, 4065, https://doi.org/10.1038/s41598-017-04455-5.

Simoncelli, S., N. Pinardi, C. Fratianni, C. Dubois, and G. Notarstefano, 2018: Water mass formation processes in the Mediterranean Sea over the past 30 years. In: Copernicus Marine Service Ocean State Report, Issue 2. *Journal of Operational Oceanography*, **11**(Sup1), s1–s142.

Simoncelli, S., F. Reseghetti, C. Fratianni, L. J. Cheng, and G. Raiteri, 2024: Reprocessing of eXpendable BathyThermograph (XBT) profiles from the Ligurian and Tyrrhenian seas over the time period 1999–2019 with a full metadata upgrade. *Earth System Science Data*, **16**, 5531–5561, https://doi.org/10.5194/essd-16-5531-2024.

Simoncelli, S., and Coauthors, 2025: Strengthening the ocean data expert's community for timely and high-quality data provision. *Bull. Amer. Meteor. Soc.*, **106**, E1589–E1600, https://doi.org/10.1175/BAMS-D-25-0143.1.

Simpkins, G., 2024: Drivers of Southern Ocean cooling. *Nature Reviews Earth & Environment*, **5**, 4, https://doi.org/10.1038/s43017-023-00513-x.

Stokes, C. R., J. L. Bamber, A. Dutton, and R. M. DeConto, 2025: Warming of +1.5°C is too high for polar ice sheets. *Communications Earth & Environment*, **6**, 351, https://doi.org/10.1038/s43247-025-02299-w.

Storto, A., and C. X. Yang, 2024: Acceleration of the ocean warming from 1961 to 2022 unveiled by large-ensemble reanalyses. *Nature Communications*, **15**, 545, https://doi.org/10.1038/s41467-024-44749-7.

Storto, A., S. Masina, and A. Navarra, 2016: Evaluation of the CMCC eddy-permitting global ocean physical reanalysis system (C-GLORS, 1982–2012) and its assimilation components. *Quart. J. Roy. Meteor. Soc.*, **142**, 738–758, https://doi.org/10.1002/qj.2673.

Szekely, T., J. Gourrion, S. Pouliquen, and G. Reverdin, 2024: CORA, Coriolis Ocean Dataset for Reanalysis. *SEANOE*, https://doi.org/10.17882/46219.

Tan, Z. T., K. von Schuckmann, S. Speich, L. Bopp, J. Zhu, and L. J. Cheng, 2025b: Observed large-scale and deep-reaching compound ocean state changes over the past 60 years. *Nature Climate Change*, https://doi.org/10.1038/s41558-025-02484-x.

Tan, Z. T., L. J. Cheng, V. Gouretski, B. Zhang, Y. J. Wang, F. C. Li, Z. H. Liu, and J. Zhu, 2023: A new automatic quality control system for ocean profile observations and impact on ocean warming estimate. *Deep Sea Research Part I: Oceanographic Research Papers*, **194**, 103961, https://doi.org/10.1016/j.dsr.2022.103961.

Tan, Z. T., and Coauthors, 2025a: CODC-S: A quality-controlled global ocean salinity profiles dataset. *Scientific Data*, **12**, 917, https://doi.org/10.1038/s41597-025-05172-9.

Thomas, A. P., and W. Liu, 2025: Ocean circulation change modulates tropical atmospheric circulation in a warming climate: The role of ocean heat uptake. *J. Climate*, **38**, 5305–5321, https://doi.org/10.1175/JCLI-D-24-0228.1.

Trenberth, K. E., 2011: Changes in precipitation with climate change. *Climate Research*, **47**, 123–138, https://doi.org/10.3354/cr00953.

Trenberth, K. E., A. Dai, R. M. Rasmussen and D. B. Parsons, 2003: The changing character of precipitation. *Bull. Amer. Meteor. Soc.*, **84**, 1205–1217, https://doi.org/10.1175/BAMS-84-9-1205.

Trenberth, K. E., J. T. Fasullo and M. A. Balmaseda: 2014: Earth's energy imbalance. *J. Climate*, **27**, 3129–3144, https://doi.org/10.1175/JCLI-D-13-00294.1.

Trenberth, K. E., L. J. Cheng, P. Jacobs, Y. X. Zhang, and J. Fasullo, 2018: Hurricane Harvey links to ocean heat content and climate change adaptation. *Earth's Future*, **6**, 730–744, https://doi.org/10.1029/2018EF000825.

Trenberth, K. E., L. J. Cheng, Y. Y. Pan, J. Fasullo, and M. Mayer, 2025: Distinctive pattern of global warming in ocean heat content. *J. Climate*, **38**, 2155–2168, https://doi.org/10.1175/JCLI-D-24-0609.1.

von Schuckmann, K., and P.-Y. Le Traon, 2011: How well can we derive Global Ocean Indicators from Argo data?. *Ocean Science*, **7**, 783–791, https://doi.org/10.5194/os-7-783-2011.

Von Schuckmann, K., and Coauthors, 2016: The Copernicus marine environment monitoring service ocean state report. *Journal of Operational Oceanography*, **9**, s235–s320, https://doi.org/10.1080/1755876X.2016.1273446.

von Schuckmann, K., and Coauthors, 2020: Heat stored in the Earth system: Where does the energy go?. *Earth System Science Data*, **12**, 2013–2041, https://doi.org/10.5194/essd-12-2013-2020.

von Schuckmann, K., and Coauthors, 2023: Heat stored in the Earth system 1960-2020: where does the energy go?. *Earth System Science Data*, **15**, 1675–1709, 2023. https://doi.org/10.5194/essd-15-1675-2023.

Xie, S.-P., H. Annamalai, F. A. Schott, and J. P. McCreary Jr., 2002: Structure and mechanisms of south Indian Ocean climate variability. *J. Climate*, **15**, 864–878, https://doi.org/10.1175/1520-0442(2002)015<0864:SAMOSI>2.0.CO;2.

Yin, X. G., and Coauthors, 2024: NOAAGlobalTemp Version 6: An AI-based global surface temperature dataset. *Bull. Amer.*

Meteor. Soc., **105**, E2184–E2193, https://doi.org/10.1175/BAMS-D-24-0012.1.

Yu, L. S., and R. A. Weller, 2007: Objectively analyzed air–sea heat fluxes for the global ice-free oceans (1981–2005). *Bull. Amer. Meteor. Soc.*, **88**, 527–540, https://doi.org/10.1175/BAMS-88-4-527.

Zhang, B., and Coauthors, 2024a: CODC-v1: A quality-controlled and bias-corrected ocean temperature profile database from 1940–2023. *Scientific Data*, **11**, 666, https://doi.org/10.1038/s41597-024-03494-8.

Zhang, M., L. Chen, N. Xu, and G. Z. Cao, 2024b: Influences of earth incidence angle on FY-3/MWRI SST retrieval and evaluation of reprocessed SST. *Journal of Tropical Meteorology*, **30**, 230–240, https://doi.org/10.3724/j.1006-8775.2024.021.

Zhang, R. W., X. Wang, and C. Z. Wang, 2018: On the simulations of global oceanic latent heat flux in the CMIP5 multimodel ensemble. *J. Climate*, **31**, 7111–7128, https://doi.org/10.1175/JCLI-D-17-0713.1.

Zhang, R. W., W. H. Guo, X. Wang, and C. Z. Wang, 2023: Ambiguous variations in tropical latent heat flux since the years around 1998. *J. Climate*, **36**, 3403–3415, https://doi.org/10.1175/JCLI-D-22-0381.1.